FEM–DEM modeling of pseudo static experiments on scaled-down rockfill dams with dry stone pitching

Ali Haidar, Eric Vincens, Fabian Dedecker, Roland Plassart

Received: Added at production | Revised: Added at production | Accepted: Added at production

DOI: xxx/xxxx

ARTICLE TYPE

FEM-DEM modeling of pseudo static experiments on scaled-down rockfill dams with dry stone pitching

Ali Haidar[1,2] | Eric Vincens*[1] | Fabian Dedecker[2] | Roland Plassart[3]

[1]Ecole Centrale de Lyon, LTDS, UMR CNRS 5513, Université de Lyon, 36 Avenue Guy de Collongue, 69134 Ecully, France
[2]ITASCA Consultants SAS, 29 Ave. Joannès Masset, 69009 Lyon, France
[3]EDF Hydro – Centre d'Ingénierie Hydraulique, 10 Allée du Lac de Tignes, 73290 La Motte-Servolex, France

Correspondence
*Eric Vincens, Ecole Centrale de Lyon, LTDS, UMR CNRS 5513, Université de Lyon, 36 Avenue Guy de Collongue, 69134 Ecully, France. Email: eric.vincens@ec-lyon.fr

Abstract

Rockfill dams with stone pitching are specific hydraulic structures generally built in the early XXth century where stones used to be hand-placed without mortar to constitute the upward and downward dam faces. Few studies have been carried out to quantify the specific and critical role of the pitching in the dam stability against both static and seismic forces.

Herein, a numerical model is proposed to model pseudo-static tests performed on four different scaled-down rockfill dams with a stone pitching. A mixed FEM-DEM approach is used, and two different constitutive models were considered for the backfill. A validation of the numerical model is firstly proposed based on the scaled-down tests. Then, the stone pitching displacement profiles and the dams safety factors against failure are analyzed and compared for the four studied cases. This study allows qualitative conclusions to be drawn and pave the way to upcoming investigations on actual structures of the same kind.

KEYWORDS:
stone, DEM, FEM, retaining structure, seismic

1 | INTRODUCTION

Dry-stone structures are one of the first known and executed projects by human beings in civil engineering history[1]. They can be found worldwide as soon as the resource was available. Most famous and known examples of this heritage are "Stonehenge" in England, the "Iron Age Brochs" in Scotland (Thew et al. 2013)[2], the "Great Zimbabwe" in Zimbabwe, and more recently "Machu Picchu" in Peru. In France, "Pont du Gard" is considered the most symbolic dry-stone structure.

Particularly, rockfill dams with dry-stone pitching on downstream and upstream faces are specific and remarkable structures among this heritage (Figure 1). They hold an inner backfill generally made of decametric blocks and faces on both the upstream and downstream faces made of carefully hand-placed rubble or cut stones. This type of structure seemed to have appeared at the beginning of the pyramid age (around 2600 BC) in Egypt[3]. EL-Kafara dam in Egypt is the oldest known water-retaining structure of such a size in the world. The design of those dams may differ from country to country in which, sometimes, dumped rockfill zones for the backfill were mixed with hand-placed rockfill zones[4]. In the panel of more recent rockfill dams built in the XX century, two different designs co-exist for the backfill: one typical of Italy and other mainly developed in the USA. For example, in Italy, the rockfill of the backfill could be totally hand-placed due to the availability of an abundant and inexpensive qualified workforce. In the USA, the rockfill was generally hand-placed only under the upstream face due to the scarcity of skilled masons. This minimum structured and dense layer was required to facilitate the construction of the dry-stone pitching while providing a better stability for it.

TABLE 1 Rockfill dams built in France from 1940 to 1960

Date	Dam	Height	Date	Dam	Height
1942	Araing	25 m	1951	Chammet	19.3 m
1943	Laurenti	15 m	1951	Greziolles	30 m
1949	Grandes Pâtures	20 m	1952	Saint-Nicolas	6 m
1950	Auchaize	6 m	1953	Escoubous	20 m
1950	Portillon	22.5 m	1953	Les Laquets	13 m
1950	Vieilles Forges	10 m	1959	La Sassière	30 m

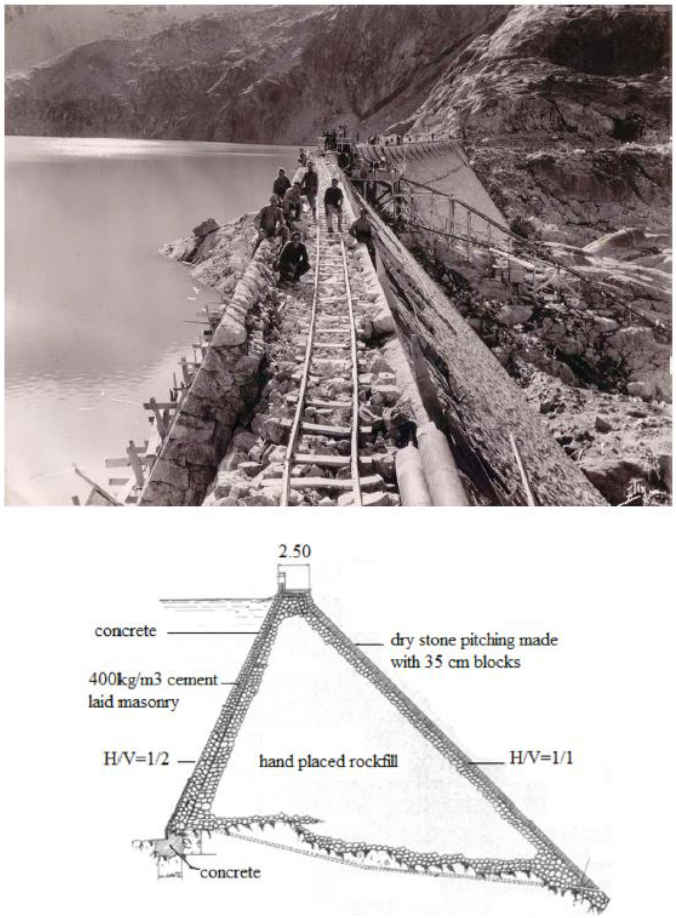

FIGURE 1 Example of a typical rockfill dam built with hand-placed rockfill: photography of the construction and cross-section (courtesy of EDF)

In France, between 1940 and 1960, during and after World War II, a period when workforce was at low cost, twelve rockfill dams were built (Table 1). They were mainly based on the USA design but with some Italian peculiarities such as the steep downstream fruit and faces protected by a dry stone pitching. Most of those dams are still operated by the French stakeholder "Electricity of France" '(EDF). A snapshot of the construction site just before the installation of the stones at crest and a typical cross-section of such rockfill dam are given in Figure 1a and Figure 1b respectively. The mechanical behaviour and the justification of the stability of such dams against the seismic motion are not definitively established.

In the past, several experimental campaigns on dry-stone structures were carried out to provide a better understanding of their mechanical behavior. The first reported studies dated back to the XIXth century when Anon[5] in 1845 and Burgoyne[6] in 1853 studied different features concerning dry stone retaining walls (DSRWs). More recently, new full scale experiments were

carried out in France to get new recommendations for the design of DSRWs such as Colas et al. (2010-2013)[7,8] and Villemus et al. (2006)[9]. On the other hand, Mundel et al. (2009,2010)[10,11] conducted full scale experiments in Great Britain to understand the origin of the bulging phenomenon observed on site that leads most of old DSRWs to failure. In addition, Savalle (2020)[12] carried out scaled-down experiments to study the seismic behaviour of DSRWs. Finally, EDF funded an experimental campaign (denoted herein PEDRA experimental campaign) involving scaled-down physical models of rockfill dam with dry stone pitching to study the role of the pitching properties in the stability of the dam. A detailed description of this latter campaign is given in Section 2.

All those experiments on dry-stone structures allowed to constitute an extensive database for the validation of analytical design tools including the homogenized yield theory (Colas et al.[13,14]) and other analytical tools (Alejano et al. 2012[15,16], Kim et al. 2011[17], Terrade et al. 2018[18]). It also allowed to validate numerical models[19,20,21]. In 2004, Deluzarche[22,21] modeled a full scale dam using a fully discrete element method (DEM)[23,24] and proved the key role of the dry-stone pitching on the stability of the rockfill dam. This study was very innovative at the time but limited as they did not provide any validation of the approach. Moreover, this study was based on a 2-dimensional computation with a gross modeling of the pitching. Another study was carried out by Chen in 2012[25]. He used a 3-dimensional continuum approach to model a concrete faced rockfill dam using two different constitutive models (Mohr-Coulomb and LK-Enroch which is a complex constitutive law developed by EDF to model the mechanical behavior of rockfill). He proved the importance of the use of sophisticated constitutive models to correctly retrieve pathologies observed on such structures.

A fully DEM approach allows large relative displacements between individual bodies to be taken into account precisely which may be the case for actual dry stone structures but is generally computation time consuming. In the case of DSRWs, Oetomo in 2013-2016[19,26,20] showed that such approach can advantageously be substituted by a mixed discrete-continuum (FEM-DEM) approach where the backfill is modeled by a continuum approach while the dry-stone wall by a DEM approach. Both models were able to retrieve results found with full-scale experiments on DSRWs with a very good precision but gain of much computational time was obtained with the mixed FEM-DEM approach.

In this paper, a mixed FEM-DEM approach is used to model the experimental campaign funded by EDF and involving scaled-down rockfill dam with dry-stone pitching. The dam body (rockfill) is modeled as a continuum body and the stone pitching as a discrete system. The main objective of the study is to validate the numerical approach to study the mechanical behavior of such structure. A second objective is to study the effect of stone pitching characteristics (kind of material, density, assemblage) on their resistance. The modeling of full scale rockfill dams with dry stone pitching is out of the scope of this work.

2 | PEDRA EXPERIMENTAL CAMPAIGN

2.1 | Objective

This campaign was motivated by the lack of robust database to validate numerical models for rockfill dam with dry stone pitching such as the one developed by Deluzarche[22,21]. Considering different materials and techniques for building the pitching in existing EDF rockfill dams, scaled-down dams were designed then tilted to evaluate their pseudo-static resistance. The pseudo-static approach is a simplified approach to qualify the seismic resistance of structures where the inertial induced forces by the seismic motion to the structures are modeled by constant forces (e.g. european standard EUROCODE 8).

2.2 | Studied cases

The shape and dimensions of the physical models are inspired by a specific dam operated by EDF, with a down-scale of 1/10. It is a structure of 2m in height, 4.2m in length and 2.25m in width with a slope of 45° on both faces (Figure 2). These models were built inside a bucket of a crane tuck. The pseudo-static experiments were carried out by the rotation of the bucket using the crane truck until dam failure. This rotation will lead to forces acting horizontally on the dam which will eventually break the dam and the pitching which is the state of failure. Higher tilting failure angle means the structure can bear higher horizontal destabilizing forces which leads to the fact that it is more resistant.. An example of the physical model is shown in Figure 2. Steel plates were welded on the 2 internal sides of the bucket and then covered with a polyane sheet to limit friction between the dam structure and the side walls. Two steel rods were welded to the base of the truck to maintain the first row of stone pitching at both face toe (upstream and downstream faces).

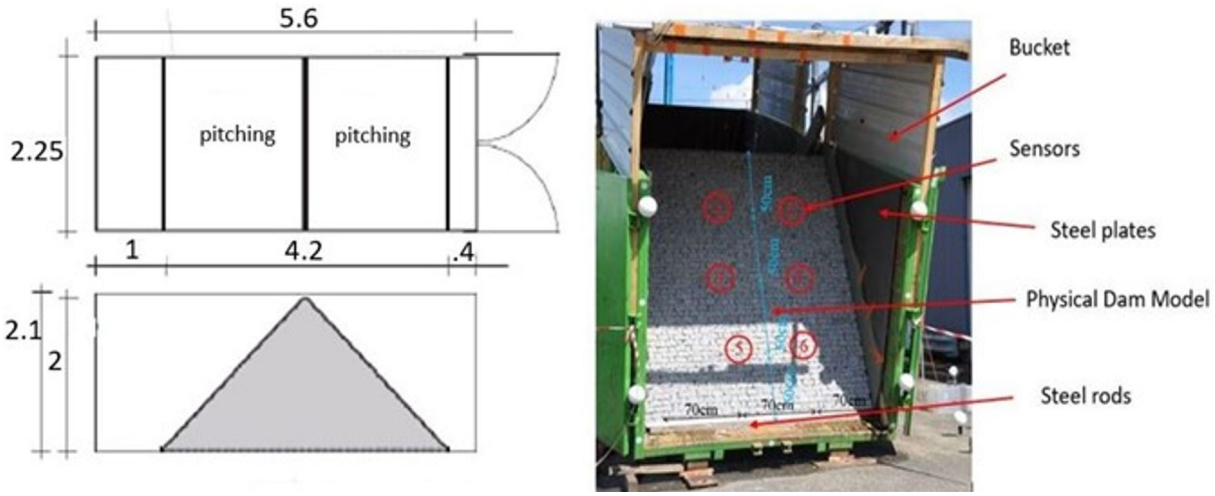

FIGURE 2 Example of the PEDRA scaled-down physical model and its dimensions

FIGURE 3 Dry-stone pitching of the four physical models in PEDRA experimental campaign

Four different dam models with dry-stone pitching were built and tilted. All four models had identical dimensions and a dam body consisting of a rockfill with a uniformity coefficient of 2 and a porosity of approximately 0.45. The rockfill grading ranges from 10mm to 80mm with a D_{50} of 40mm. The difference between the four cases lied in the dry-stone pitching: the four cases differed according to the pitching surface density (pitching with one or two stone layers), material (granite or schist), assemblage (ordered or disordered, anchorage of stones in the backfill) and stone dimensions (Figure 3) although some of them may have shared common features (Table 2). In addition, to justify the role played by the dry-stone pitching in the dam stability, an experiment involving a scaled-down rockfill dam without pitching (1m in height) was carried out.

Six sensors were fixed on the downstream dry stone pitching to track the dam displacements. They were distributed on the top, middle and upper part of it (Figure 2). In addition, photogrammetry using four cameras and a 3D laser scanner were used to localize deformations of all the stones during the rotation process. A high speed camera was also used to better track the pitching kinematics at failure. The failure tilting angles for the four cases are given in Table 3. Herein, the sensors' displacements and

TABLE 2 Four cases studied in PEDRA experiments

	Case 1	Case 2	Case 3	Case 4
Stone pitching type	Granite (1 layer)	Ordered Schist	Disordered Schist with anchorage	Granite (2 layers)
Surface density	115 kg/m^2	114 kg/m^2	177 kg/m^2	230 kg/m^2
Stone thickness	5.6 cm	5 cm	5 to 12 cm	11.2 cm
Stone height	5.6 cm	5 cm	3 to 25 cm	5.6 cm
Stone width	5 and 10 cm	3 to 40 cm	3 to 40 cm	5 and 10 cm
Stone friction angle (Slip tests)	29°	26.5°	26.5°	29°

pitching deformations are just given for case 4 (Figure 4) but the results are typical of those found for the other cases. One can note that failure was not according to a perfect plane strain mode due to restrictions of movement at lateral end sides in spite of care in the design of the system. Similar features were observed in the case of experiments on DSRWs but repeatability tests showed that they do not play a significant role in the quantitative aspects of the problem (Savalle, 2020)[12].

2.3 | Main results

By comparing the results of the four studied cases, several conclusions can be drawn:

- The comparison between case 1 and case 2 (similar pitching weight) shows that a higher friction angle (29° for granite against 26.5° for the schist) leads to a higher dam resistance;
- The comparison between case 1 and case 4 (the pitching is formed of a layer of granite for case 1 and two layers for case 4) shows that the pitching weight is a significant parameter explaining the dam resistance;
- Case 3 shows that pitching anchorage in the backfill increases the dam resistance.

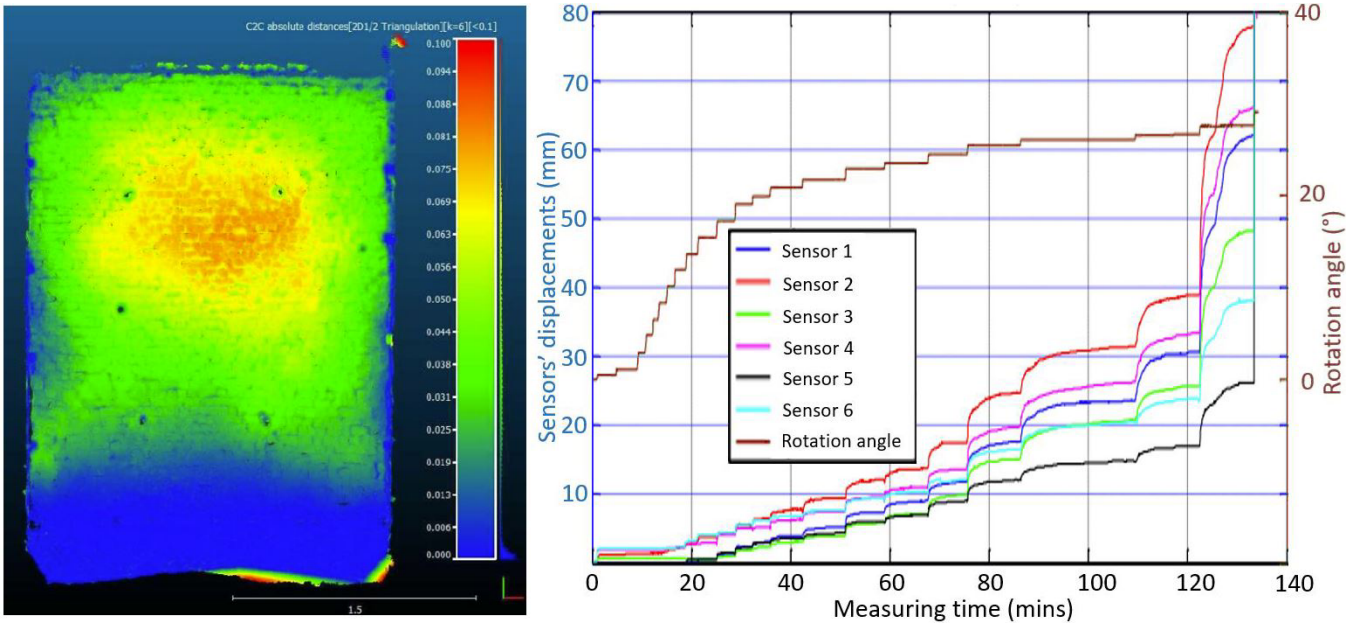

FIGURE 4 Dry stone pitching deformations of case 4 at bucket rotation angle of 27° (just before failure) and sensor time displacements as a function of the bucket rotation angle

TABLE 3 Failure tilting angle for the four studied experimental cases

	Case 1	Case 2	Case 3	Case 4
Failure angle	24°	21°	29.5°	28°
Bucket rotation angle (Failure angle + dam slope (45°))	69°	66°	74.5°	73°

3 | NUMERICAL MODEL

3.1 | System

All the cases involved in PEDRA experimental campaign were modeled numerically. The dam body (rockfill) was modeled as a continuum medium using *FLAC3D* whereas the dry-stone pitching was modeled as a discrete system using *PFC3D*. Both commercial software are developed by ITASCA[24] and can be easily coupled one to each other to share information. Herein, information is shared and transferred at pitching-backfill interface. The four numerical models associated to the four PEDRA cases are given in Figure 5. Their dimensions are the same as in the experiments (2m in height, 4.2m in length and 2.25m in width). The dry stone pitching is modeled by regular perfect parallelepipedic blocks whose dimensions correspond to the average stone dimensions in each case (Figure 6).

To simulate the two lateral sides of the bucket, namely two smooth plates covered with a polyane sheet (to limit friction), the normal displacement (y-direction in Figure 7) of the backfill vertical planes was fixed and a no-friction condition was applied. The dam foundation was fixed in all directions and a frictional interface was used between the dam base and its foundation. Concerning the stone pitching, the first row of stones at dam toe on both upstream and downstream faces was totally fixed to simulate the presence of the steel rods. Moreover, the normal displacement (y-direction in Figure 7) of stones at both lateral ends of the pitching was also fixed as done for the backfill (Figure 7).

The computation was divided into several successive steps. The first step consisted of the creation of the dam body with its geometry within *FLAC3D* and then the mesh for the backfill was generated. Gravity was applied until equilibrium is reached: equilibrium is supposed to be obtained when the ratio between the unbalanced forces and the total forces is smaller than 1.10^{-5}. Then, the dry-stone pitching was generated within *PFC3D* on the upstream and downstream faces of the dam. At this stage, the

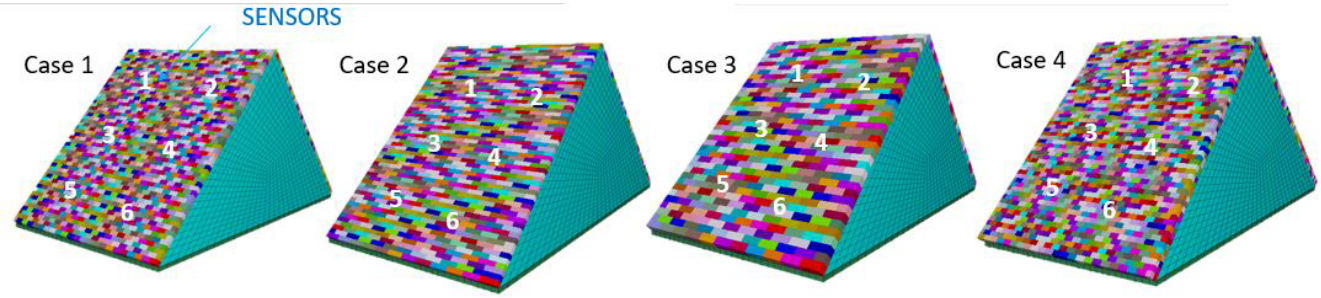

FIGURE 5 Numerical models of the four PEDRA cases

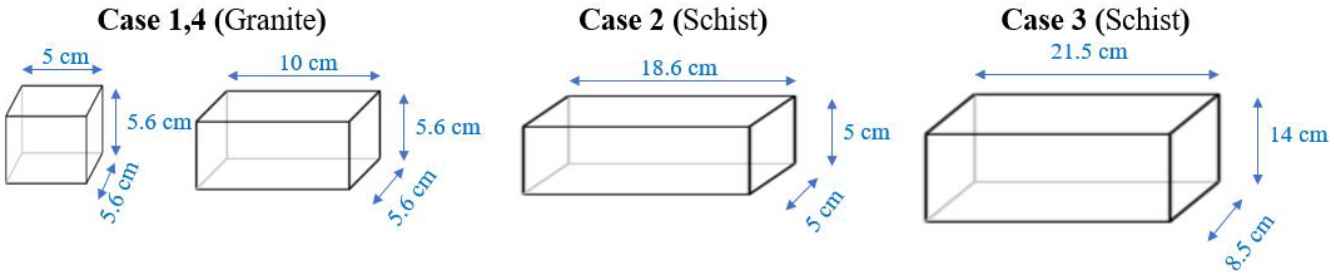

FIGURE 6 Dimensions of the dry-stone pitching used in the numerical model

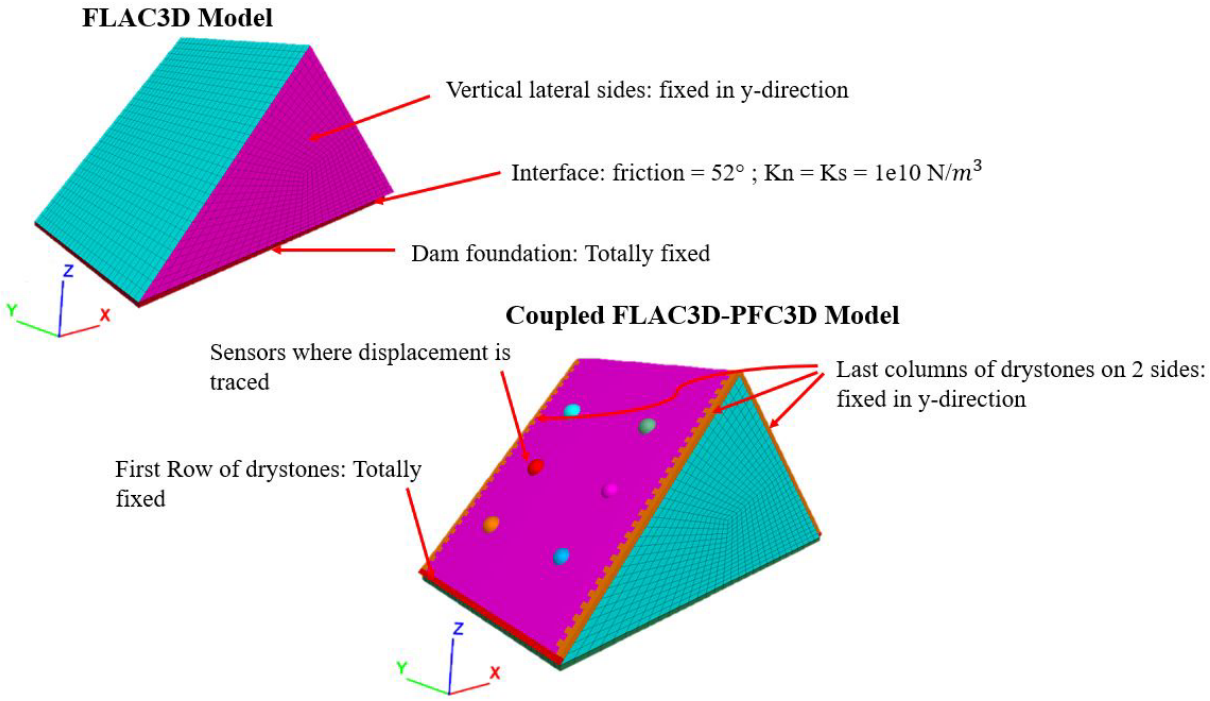

FIGURE 7 Boundary conditions of the numerical model

coupling between the two softwares is processed by creating an interface wall between the stone pitching and the dam body. The full dam model is run again under gravity to reach a new mechanical equilibrium. All mechanical properties of the dam as well as of the pitching-backfill interface are discussed hereafter in section 4.

After building the whole model, the pseudo static test (tilting test) was modeled by rotating the dam: rotation is simulated by rotating the gravity vector in the vertical (X,Z) plane (Figure 7). The dam is rotated with an increment of 1° until failure is obtained (the designed failure criteria developed for this study are described in the next subsection). During the rotation process, the displacements at points corresponding to the location of the six PEDRA sensors were recorded. The whole computation process is shown in details in Figure 8.

The dam body mesh (backfill) was defined by studying the effect of the mesh size on the failure angle and on the maximum displacement of the pitching at a given rotation angle of 20°. The main goal was to find the minimum needed mesh size (gridpoint number) from which the mesh size had negligible effect on the results. Figure 9 shows the evolution of the failure angle and the maximum displacement as a function of the gridpoint number on the backfill face in contact with the stone pitching. Both curves reach a "plateau" after a certain enough high gridpoint number represented by the red dotted line. The mesh corresponding to this threshold number was chosen as an optimized mesh size that guaranteed both mesh independency of results and limited computation time. For example, in case 1, each stone is in contact with at least 1 gridpoint on the backfill surface. More specifically, each stone information is transmitted to at least one surface gridpoint forming the backfill faces. So, the total number of gridpoints on the backfill surface in contact with the pitching is higher than the total number of the stones forming the pitching.

3.2 | Equilibrium and failure criteria

FLAC3D and PFC3D solve the equation of the dynamics using an explicit time scheme. A criterion was designed to define when static equilibrium was obtained throughout the simulation of the pseudo static tests. Another criterion was designed to state when failure was obtained before a total collapse of the whole system and thus to save computation time. Failure and possible equilibrium were tested for each rotation angle increment.

The developed criteria were similar to the one used by Oetomo and Savalle[19,26,20,27] in their respective works. For a given rotation angle, the model is run (gridpoint locations and stone positions are updated) throughout a few thousands cycles. During these cycles, if the model reaches the threshold unbalanced force ratio, the model is considered at equilibrium and another

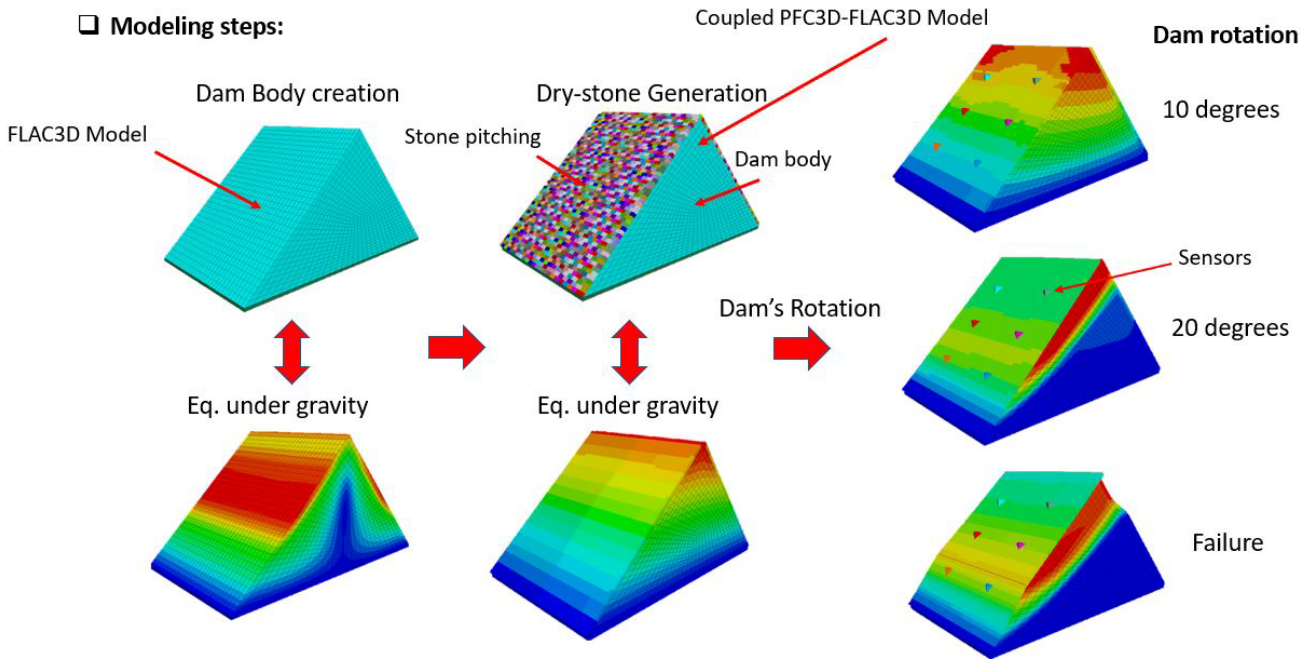

FIGURE 8 Example of the modeling procedure and steps (The displacement fields shown are just examples with only qualitative meaning and not quantitative)

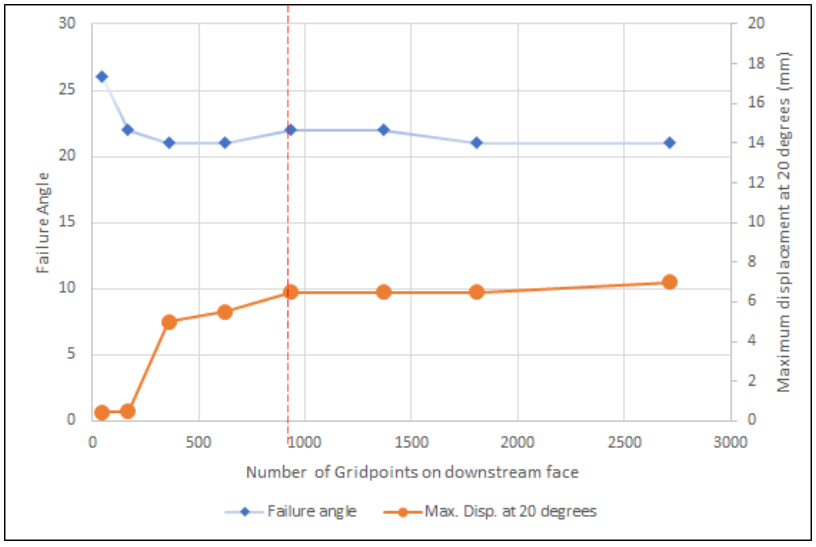

FIGURE 9 Mesh study of the *FLAC3D model*

increment of rotation angle can be processed. Otherwise, a 2nd criterion, based on the pitching kinetic energy, is checked to test if the dam has reached failure. If the kinetic energy is higher than 1.10^{-3}J for 10 consecutive measurements with 500 cycles between each, failure is supposed to have been reached. If not, it means that the model may tend to a stable state and further chance for obtaining equilibrium (few thousands more cycles) is given to the whole system. The kinetic energy threshold value was chosen during a preliminary study where the pitching kinetic energy was monitored which implies that the derived threshold value is only valid for the study system. The full scheme is given in Figure 10.

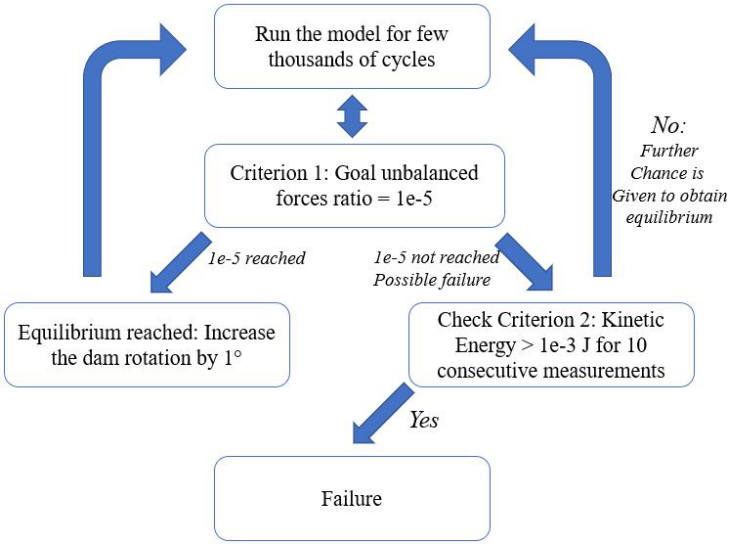

FIGURE 10 Computation scheme involving equilibrium and failure criteria

4 | MODEL CALIBRATION

Due to its simplicity, Mohr-Coulomb (MC) constitutive model was used to model the dam body as a first computation. Then, a more sophisticated constitutive model denoted LK-Enroch (LKE) developed for rockfill at EDF is used for comparison. The model parameters were calibrated using data available from PEDRA experimental campaign. When information was missing, the calibration was performed using data from the literature. The calibration process for each part of the system including backfill, stone pitching and the backfill-pitching interfaces is described in details in the following subsections.

4.1 | Backfill

The dam body is composed of a backfill made of angular granite rockfill with a grading ranging from 10mm to 80mm with a uniformity coefficient of 2 and a D_{50} of 40mm. Porosity is equal to 0.45.

4.1.1 | Mohr-Coulomb

MC model has 5 parameters to be calibrated including Young's modulus E, Poisson's ratio ν, cohesion C, internal friction angle ϕ, and dilatancy angle ψ (Appendix 1). The calibration process of the model parameters was based on experimental triaxial tests at 100kPa and 200kPa carried out during PEDRA campaign. A 1m diameter cell was used in order to achieve a Representative Elementary Volume for the considererd granular material. However, due to the small size of the scaled-down system to be modeled, the associated confining pressures are very low (between 1 to 10 kPa) and out of the range of usual confining pressures involved in triaxial tests which induced some adaptations.

LEP's chart[28] valid for rockfills was used to deduced properties at low confining pressure. The internal friction angles at 100kPa (14.5psi) and 200kPa (29psi) throughout the triaxial tests using a large cell were found equal to 42° and 39.5° respectively. These values are consistent with a rockfill at low density according to LEP's chart (Figure 11). Then, considering a low density for a poorly graded material and an average pressure ranging from 1 to 10kPa (0.15-1.5psi), the internal friction angle of the rockfill was estimated at 52°. (Table 4)

The dilatancy angle was estimated using Bolton's approach[29]. This author states that for plane strain conditions and relative density $0<I_D<0.4$, the dilatancy angle ψ_{max} can be estimated using Equation 1 which corresponds to the characteristics of the rockfill studied herein. ϕ_{peak}=52° is the peak backfill friction angle and ϕ_{crit}=38° is the critical backfill friction angle.Finally, the dilatancy angle was found close to 18°.

$$\phi_{peak} - \phi_{crit} = 0.8\psi_{max} \tag{1}$$

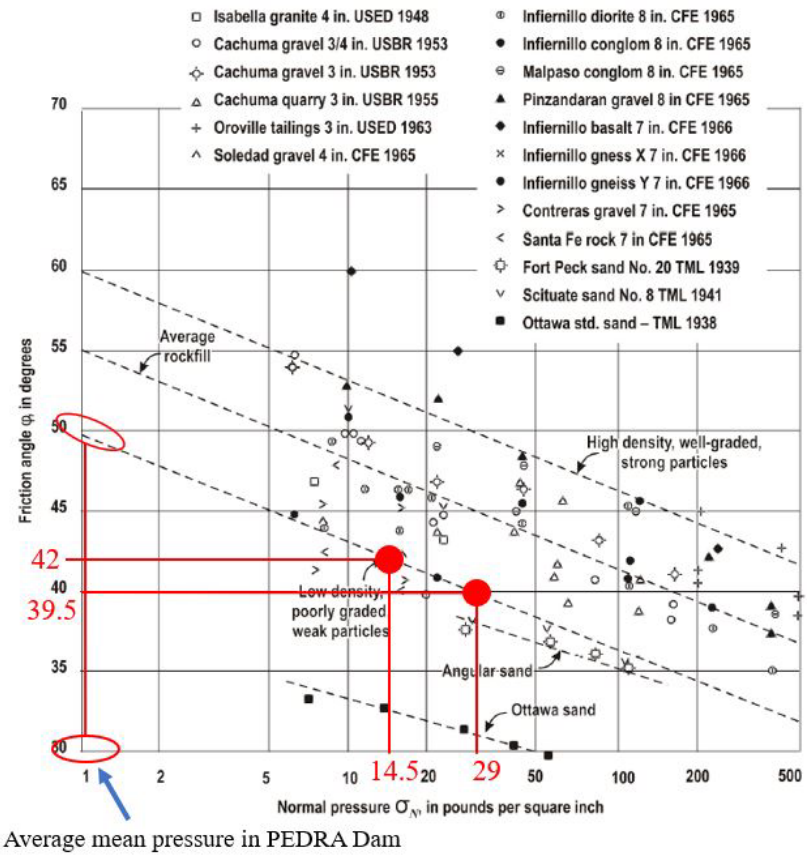

FIGURE 11 LEP'S diagram: Effect of the confining pressure on the friction angle

TABLE 4 Mohr-Coulomb parameters calibration at different confining pressures

Confining Pressure	$\phi_{peak}(°)$	$\psi(°)$	C	E(MPa)	ν
200 kPa (triaxial tests)	39	2	0	52	0.2
100 kPa (triaxial tests)	42	6	0	50	0.2
1-10 kPa (extrapolated parameters)	52	18	0	10	0.2

Finally, based on Equation 2[30] which takes into account the typical dependency of the Young's modulus with the mean pressure and considering the reference pressure P_{ref} of 100kPa[30], E_0 was identified equal to 50MPa throughout the triaxial tests with the large cell. Then, the Young's modulus at P=5kPa (average pressure in the scaled-down numerical model) was deduced. Finally, Poisson's ratio ν was kept independent of the mean pressure and cohesion C was set to zero. All the values for MC model are given in Table 4.

$$E = E_0[\frac{P}{P_{ref}}]^{0.5} \tag{2}$$

4.1.2 | LK-Enroch

LKE model is an elastoplastic model with two plastic mechanisms including an associated isotropic mechanism with isotropic hardening and a non-associated deviatoric mechanism with hardening. The isotropic mechanism is a plane perpendicular to the hydrostatic axis while the deviatoric mechanism which was designed from Hoek-Brown model corresponds to a non-straight cone centered on the hydrostatic axis. The main equations of LKE model are given in Appendix 1. This model has sixteen

parameters. As for MC model, parameters were calibrated either by using PEDRA experimental triaxial tests or using data or approaches from the literature.

LKE model takes into account the dependency of Young's modulus with the mean pressure and as described in subsection 4.1.1, E_0 was identified equal to 50MPa. Poisson's ratio ν was identified equal to 0.2 and n_{elas}= 0.5 as typically considered.

The other model parameters were identified throughout a trial-and-error technique with the help of simulations of triaxial tests. Then, considering available actual triaxial tests at 100kPa and 200kPa, both elasticity threshold parameters a_0 and m_0 were identified.

The peak threshold parameters which mainly control the value of the deviatoric stress peak are namely a_{peak}, m_{peak} and σ_c. First, the compressive strength σ_c is assumed to be equal to 100MPa[31], then a_{peak} and m_{peak} values were calibrated (Table 6) to reach the experimental deviatoric stress peak (Table 5).

Concerning the hardening parameters, $\dot{\gamma}_{peak}$ was chosen by fitting the position of the deviatoric stress peak with respect to the axial strain. $\dot{\gamma}_{res}$ and η were chosen to fit the post-peak softening phase whereas X_{ams} was chosen to fit the curvature of the pre-peak curve.

The volumetric deformations parameters were chosen with the help of the triaxial experimental volumetric curves. First, the residual friction angle ϕ_{res} equal to 38° was deduced from the actual triaxial tests. Then, the dilatancy angle ψ_0 was chosen by fitting the volumetric curves.

Finally, the isotropic mechanism parameters p_{c0} and β were estimated using Hicher and Rahma approach[30](the main equations of this approach are given in Appendix 2). While p_{c0} was identified equal to 1MPa throughout the simulations of triaxial tests, it was taken equal to 15kPa for the modeling of the scaled-down dam (average mean pressure of 5kPa). The shape form parameter γ that controls the deviatoric failure envelope dissymetry is typically taken equal to 0.87. The final values for LKE parameters are listed in Table 6.

TABLE 5 LKE peak threshold parameters calibration

	p= 200 kPa		p= 100 kPa	
	Experimental	Numerical	Experimental	Numerical
Peak deviatoric stress q (kPa)	680	690	410	400

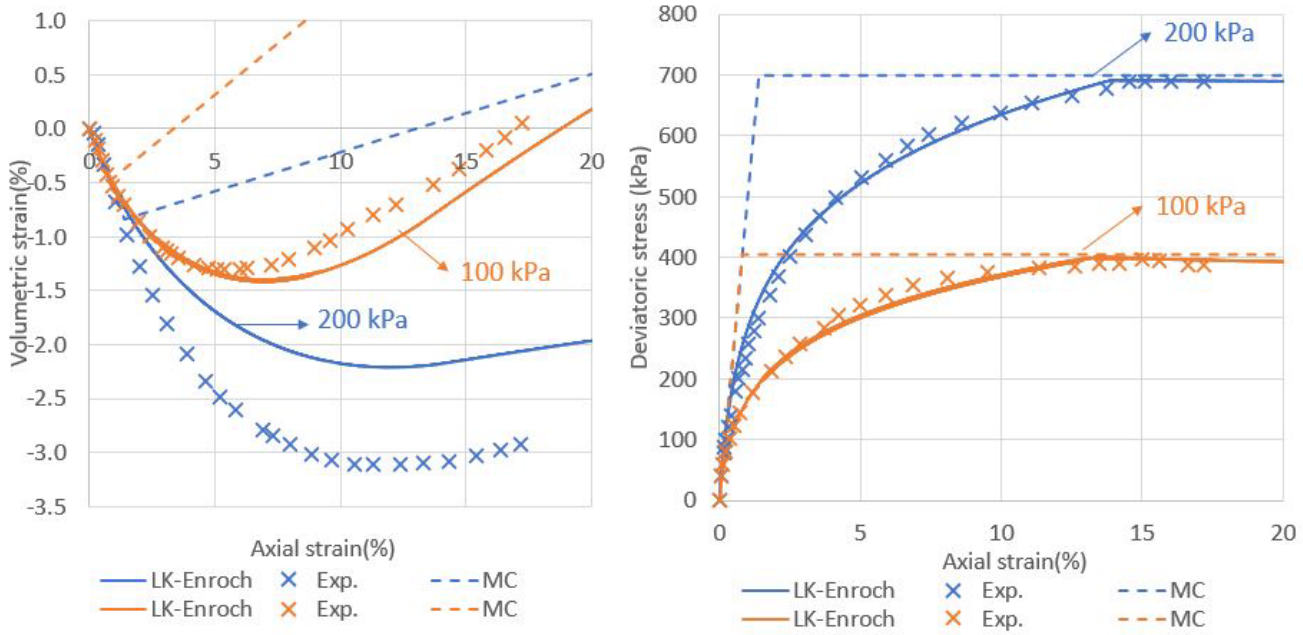

FIGURE 12 Experimental triaxial tests and simulations using MC and LKE models: deviatoric stress (right) and volumetric strain (left) at 100kPa and 200kPa

TABLE 6 Calibrated sixteen parameters of LKE model

General Parameters			
E	50E6 Pa	ν	0.2
n_{elas}	0.5	σ_c	100E6 Pa
Elasticity threshold parameters			
a_0	0.87	m_0	0.1
Peak parameters			
a_{peak} at 100/200 kPa	0.79	m_{peak} at 100/200 kPa	0.92
a_{peak} adapted to 1-10 kPa	0.815	m_{peak} adapted to 1-10 kPa	0.89
Hardening parameters			
$\dot{\gamma}_{peak}$	0.125	$\dot{\gamma}_{res}$	0.8
X_{ams}	0.005	μ	2
Volumetric deformations parameters			
ϕ_{res}	38°	ψ_0	38.5°
Isotropic mechanism parameters			
p_{c0} (scaled-down dam model)	15kPa	β	35
p_{c0} (triaxial tests)	1MPa		

The simulations of available actual triaxial tests associated to the final set of parameters for MC model and LKE model are given in Figure 12. While MC model only retrieves the main features of the curves, LKE fits in a good way the experimental triaxial curves, especially the deviatoric stress curves, which was expected. MC is typically stiffer and generates dilatancy at deformations smaller than 5%. LKE gave close volumetric strain curves in the same order of magnitude as the experiments especially at a confining pressure of 100kPa. In fact, a margin of error can be found in both the constitutive model and the experiments due to some imperfections which could lead to some small differences in some cases as found at a confining pressure of 200 kPa.

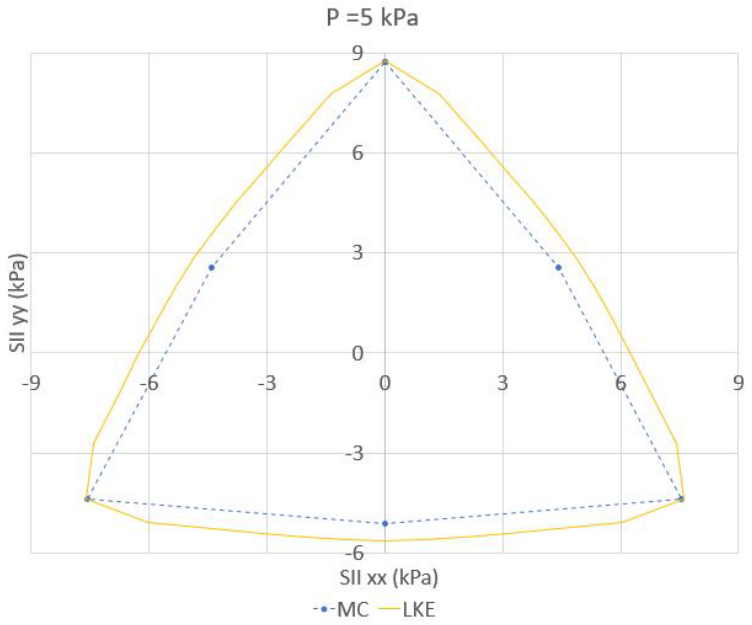

FIGURE 13 Failure envelopes of calibrated MC and LKE models at low pressures (5kPa) in the deviatoric plane

Sophisticated elastoplastic models are typically valid for the range of mean pressures associated to the calibration process (generally hundreds of kPa). Herein, the mean pressure in the scaled-down model was very different (1-10kPa) and some adaptations for the values of model parameters were considered. These adaptations allowed a better prediction of the peak strength. Then, the peak threshold parameters a_{peak} and m_{peak} were changed accordingly with a targeted value for the internal friction angle of 52° (LEP's approach[28]) as considered for the calibration of MC model. The final values of a_{peak} and m_{peak} and other LKE model parameters for the modeling of the scaled-down dams of PEDRA campaign are given in Table 6. Figure 13 gives both the failure envelopes of calibrated MC model and of LKE deviatoric mechanism in the deviatoric plane (Π plane) for a mean pressure of 5kPa.

4.2 | Dam-foundation Interface

For the modeling of the dam-foundation interface, a linear frictional Coulomb model was used. A friction angle of 52° (equal to the rockfill internal friction angle) is imposed. Normal and shear stiffnesses K_n and K_s were defined considering recommendations in $FLAC3D$ manual. For convergence reasons, stiffnesses are recommended to be ten times the equivalent stiffness K_{eq} of the most rigid zone near the interface defined by Equation 3 in which K and G are the bulk and shear modulus respectively and Δz_{min} is the minimum dimension (height) of volume element meshes at the interface. Then, the values were identified to $K_n = K_s \approx 1.10^{10}$Pa/m.

$$K_{eq} = max[\frac{(K + \frac{4}{3}G)}{\Delta z_{min}}] \tag{3}$$

4.3 | Stone pitching

Stones are modeled as infinitely rigid bodies with deformable contacts. A linear frictional law is used for the contact between blocks with several parameters including the friction coefficient, the shear stiffness and the normal stiffness. The shear and normal stiffness input can be replaced by the input of the effective modulus E^* and stiffness ratio K^* with $K^* = K_n/K_s$, K_n denoting the normal stiffness and K_s the shear stiffness.

The chosen friction coefficient μ (tangent of the friction angle of the stone-stone contact) is used for the pitching whether granite or schist. $\mu_{granite} = \tan(29°) = 0.55$ is used for the granite stones of cases 1 and 4, and $\mu_{schist} = \tan(26.5°) = 0.5$ is used for the schist stones of cases 2 and 3. The local friction angles of the granite and schist stones were obtained experimentally in PEDRA campaign. Slide slip tests were carried out by placing two stones on top of each other and a rotation of the whole system was operated until the top block slipped on the bottom one. An average value between several tests was determined for the granite and for the schist stones (Figure 14). The effective modulus and stiffness ratio used are respectively equal to 5.10^7 N/m^2 and 2. They were obtained based on a parametric study as a compromise between actual stiffness and computation times. Indeed, high stiffness induces small time increment for the resolution of the equation of the dynamics and penalize time computation. However, it is possible to reduce the contact stiffness without changing the quality of the results provided. A global damping of 0.7 which is typically used within the context of quasi static computations[23] was taken into account.

4.4 | Pitching-backfill interface

The pitching-backfill interface is activated by the coupling $PFC3D$ and $FLAC3D$ software. On both downstream and upstream faces, a coupling mechanism is processed throughout a zero thickness wall generated in $PFC3D$ whose facets coincides with the facets of the dam body in $FLAC3D$ (Figure 15). The coupling logic works by taking the contact forces and moments from the infinitely rigid bodies in $PFC3D$ (pitching stones) with wall facets and determining an equivalent force system at the facet vertices. These forces are passed to the gridpoints along with stiffness contributions to the facets of the dam body in $FLAC3D$.

The mechanical behavior at the interface between wall and dam body face can be reproduced by a purely frictional linear elastic model which is the same as the one used for the contact between blocks with the same set of parameters. For cases 1, 2 and 4, the pitching-backfill interface friction coefficient is based on the stone-stone friction coefficient[32]. Therefore, the interface friction coefficient of cases 1 and 4 (granite stones) was $\mu_{granite} = \tan(29°) = 0.55$, and of case 2 (schist) was $\mu_{schist} = \tan(26.5°) = 0.5$. In the peculiar Case 3, the pitching was anchored in the backfill. This anchorage was not modeled physically: it was considered that the shearing failure surface at the interface was shifted within the backfill due to the existence of anchors (Figure

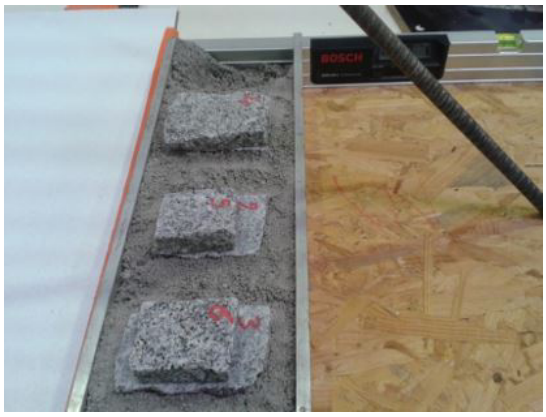

FIGURE 14 Slide test involving stones to identify friction angle

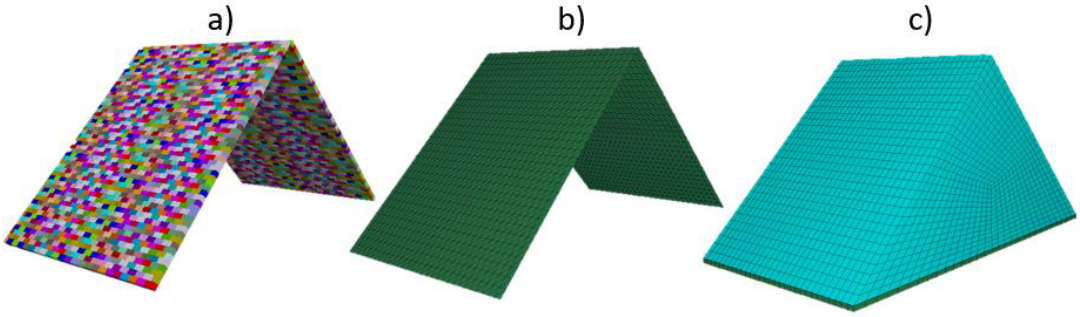

FIGURE 15 Wall zone coupling: a) stone pitching using infinitely rigid blocks, b) coupled walls at the interface, c) dam body

16). This anchorage lead to the shifting of the interface contact surface inside the backfill, a statement that is commonly taken in the case of a rough retaining wall-backfill interface. Therefore, the friction angle of the rockfill is chosen for the interface of case 3 which is $\mu_{rockfill}$= tan(52°)= 1.28. This choice of case 3 interface friction angle was also studied and validated in a previous study by Colas in 2016[32].

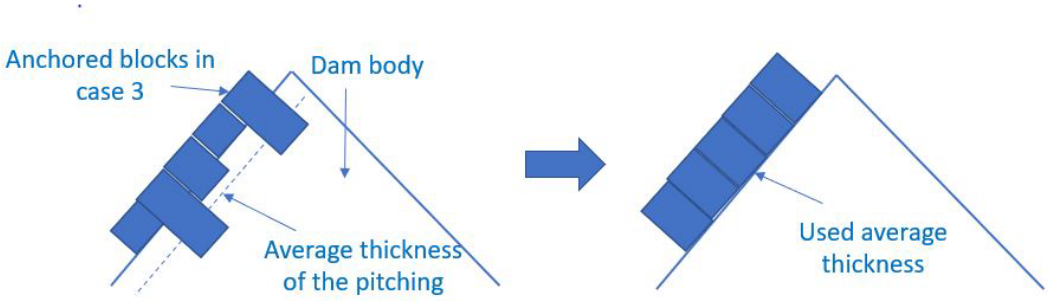

FIGURE 16 Modeling of the anchorage in case 3

5 | RESULTS AND DISCUSSION

5.1 | Validation

Figure 17 gives the failure angles of all the modeled cases using MC and LKE. Both constitutive models were able to predict the failure angle with a high quality and consequently the resistance of the scaled-down dams throughout a pseudo-static test.

The difference between the results provided by the two constitutive models lies in the displacement field. The displacements monitored in the simulation on the downstream face are compared with the ones found throughout the PEDRA experiments. Figure 18 gives the results for case 4: the displacements of the other three cases can be found in Appendix 3 (Figures 29, 30, 31). MC model underestimates displacements in most of the sensors (and cases) which was expected. Indeed, this model is characterized by a large elastic domain which generates a rigid behavior. On the contrary, LKE model is able to generate further (irreversible) deformations from small deformations due to a limited initial elastic domain that expands according to a non-linear isotropic evolution law. Moreover, LKE model was able to retrieve the evolution of the displacements with a very good accuracy.

The displacement field of the backfill and of the dry-stone pitching for case 4 (MC and LKE model) at rotation angle of 27° (just before failure) are given and compared to corresponding experimental results in Figure 19. The same scale was used between simulated and experimental results (crest is at the top of figure in Figure 19c). LKE model gave a qualitatively better prediction with respect to experiments with a more concentrated displacement field than MC model. It also holds true quantitatively.

A further analysis of the stone pitching relative displacements (rigid body displacement of the pitching was removed) was carried out in order to better understand its mechanical behavior. For this purpose, the evolution of the normal displacements along the downstream stone pitching height was traced for case 4 as a function of the rotation angle (Figure 20). The other cases show similar trends, but with different peak values and positions. The evolution of the other three cases can be found in Appendix 3 (Figures 32, 33, 34). If the zone facing the maximum displacement is located at about $0.3*H$ (H denotes height from bottom) for lower rotation angle, it stabilizes at about 40% of pitching height at failure which is also the zone where the backfill failure surface emerges on the pitching.

Figure 21 gives the normal relative displacement field (normalized by the pitching thickness) at the rotation angle just before failure along the pitching height for the four modeled cases. The normalization allows the weight of the pitching to be taken into account. Indeed, the pitching weight is one of the main properties contributing to the dam stability. This comparison leads to several conclusions about the behavior of a dry-stone pitching. A more deformable system does not mean less resistant: case 1 that generated larger relative displacements failed for a rotation angle of 25° while case 2, for a rotation angle of 23°. Accordingly, case 3 failed with a rotation angle of 30° while case 4, 28°. Moreover, as the pitching thickness increases, the peak normalized relative displacement before failure decreases; the system is stiffer. It is true for cases 3 and 4 which are thicker than cases 1 and 2.

From the same figure, it is also interesting to compare the position of the maximum relative displacement (position of the failure surface that emerges on the pitching surface). Cases 1 and 4 have the same interface friction angles and their failure

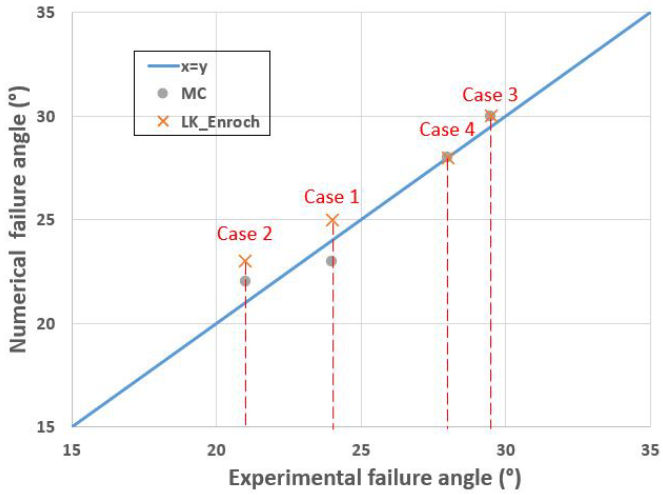

FIGURE 17 Failure angles for the four cases using MC and LKE model

position is approximately at about 0.4*H. Case 2 has a slightly lower interface friction angle which leads to a slightly lower failure position at about 0.35*H. Case 3 is the only case having much higher interface friction angle due to the pitching stone's anchorage within the dam body: the failure position is at about 0.55*H. The increase in the interface friction angle could lead to more sliding resistance at interface between the pitching and the backfill. This may cause less displacements at the bottom part of the backfill and eventually would shift the failure to a higher position of the pitching where the resistance between its blocks is lower. In fact, the higher the position of the pitching blocks, the lower their resistance due to lower normal confining forces between them. ????????

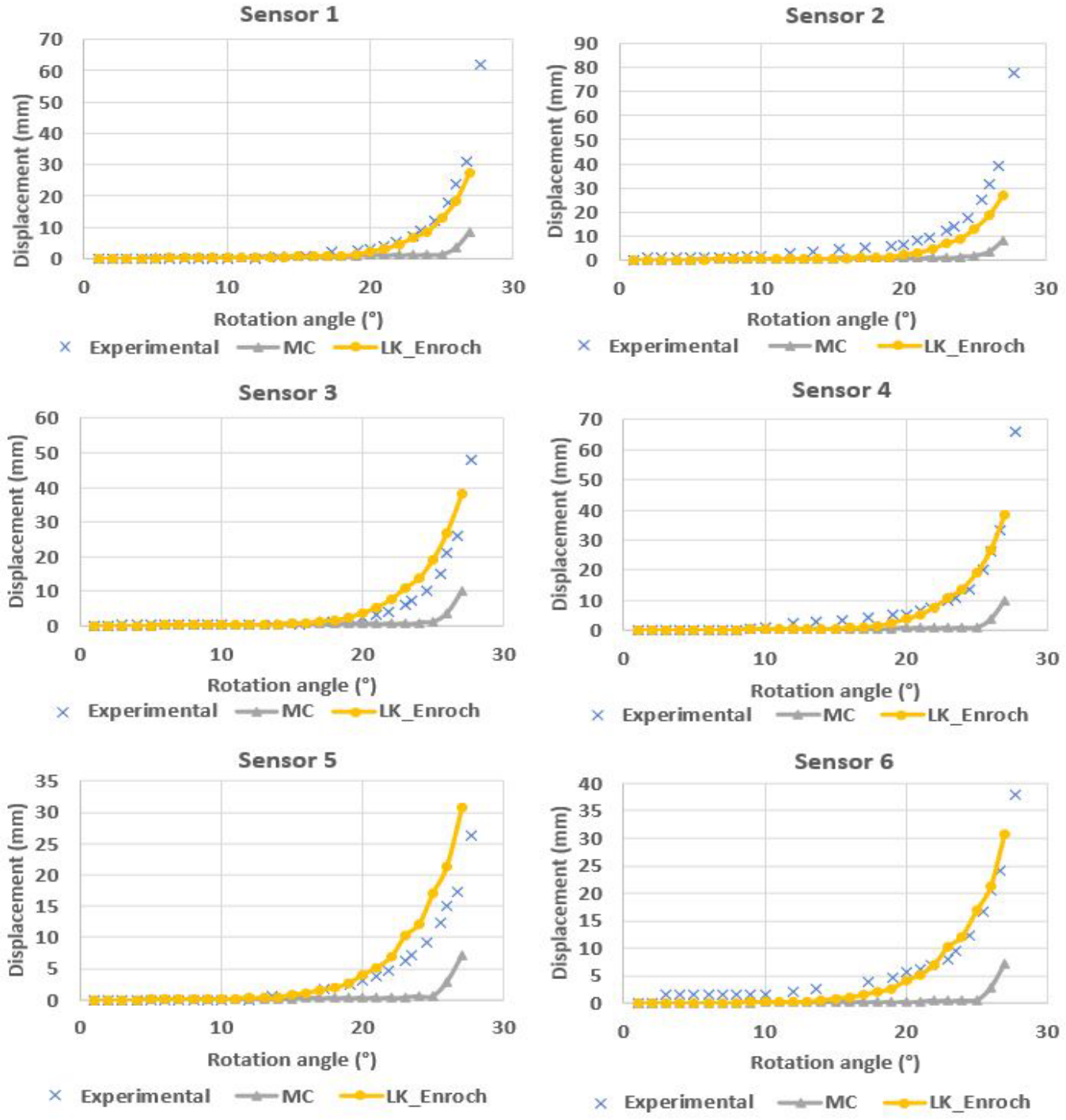

FIGURE 18 Displacements at the 6 sensors on the downstream face; case 4

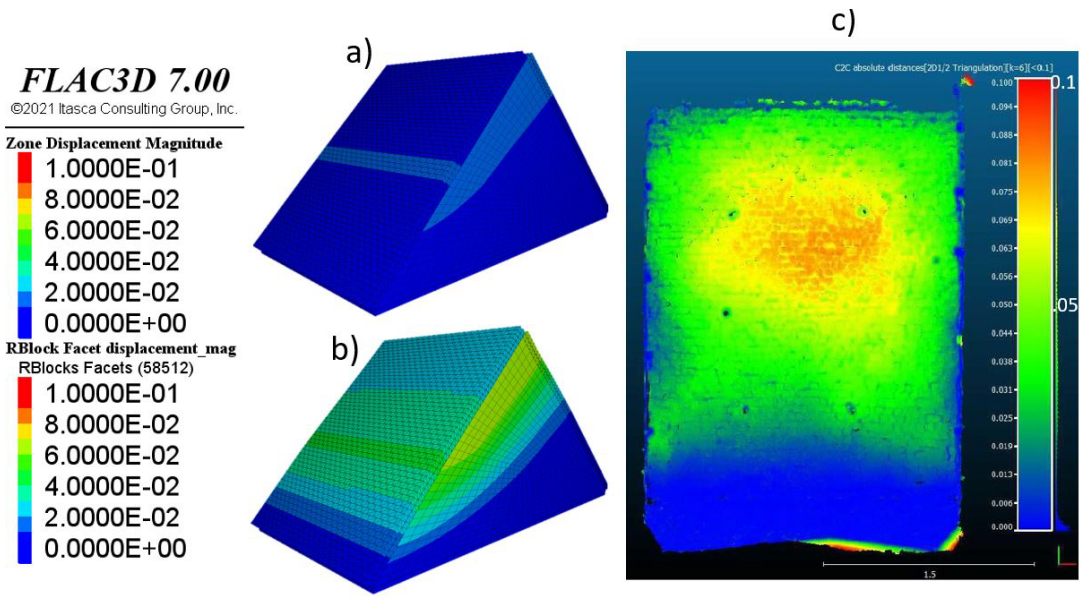

FIGURE 19 Displacements contour of the backfill and stone pitching for case 4 at rotation angle of 27° (just before failure): a) using MC, b) using LKE and c) experimentally

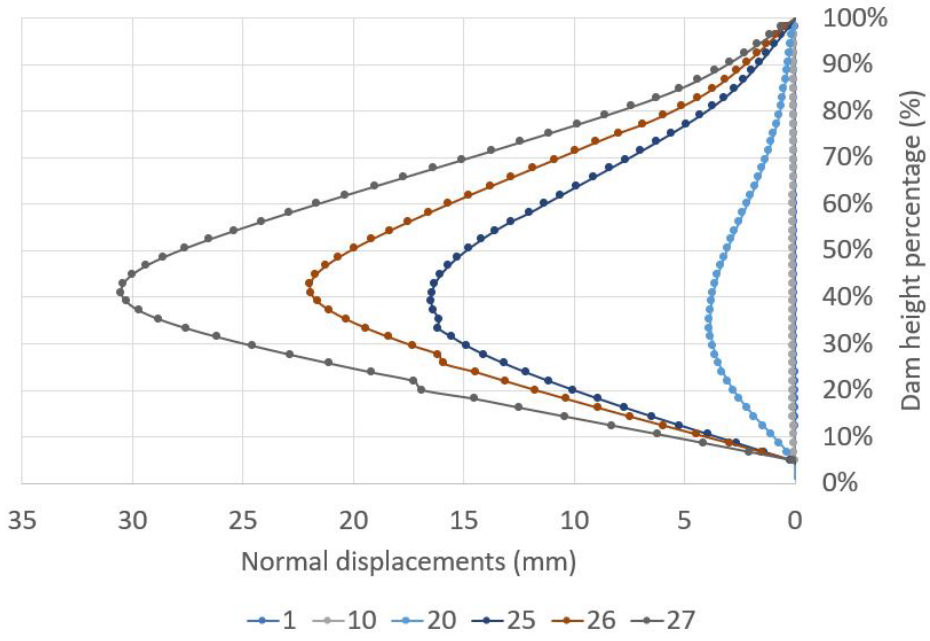

FIGURE 20 Normal relative displacements evolution of the pitching throughout the tilting tests; simulation of case 4

5.2 | Safety factors

The evaluation of the safety factors is an important step in the process of justification and design of any structure including dams. Two types of safety factors have been computed: the rotational safety factor (related to the resistance to horizontal inertial forces such as earthquakes) and the static safety factor.

The first safety factor F_θ is obtained by the rotation of the dam (pseudo-static test) as related in previous sections. This factor is defined by Equation 4 in which α is the angle of the dam slope (herein, 45°) and $\theta_{failure}$ is the angle of rotation at failure.

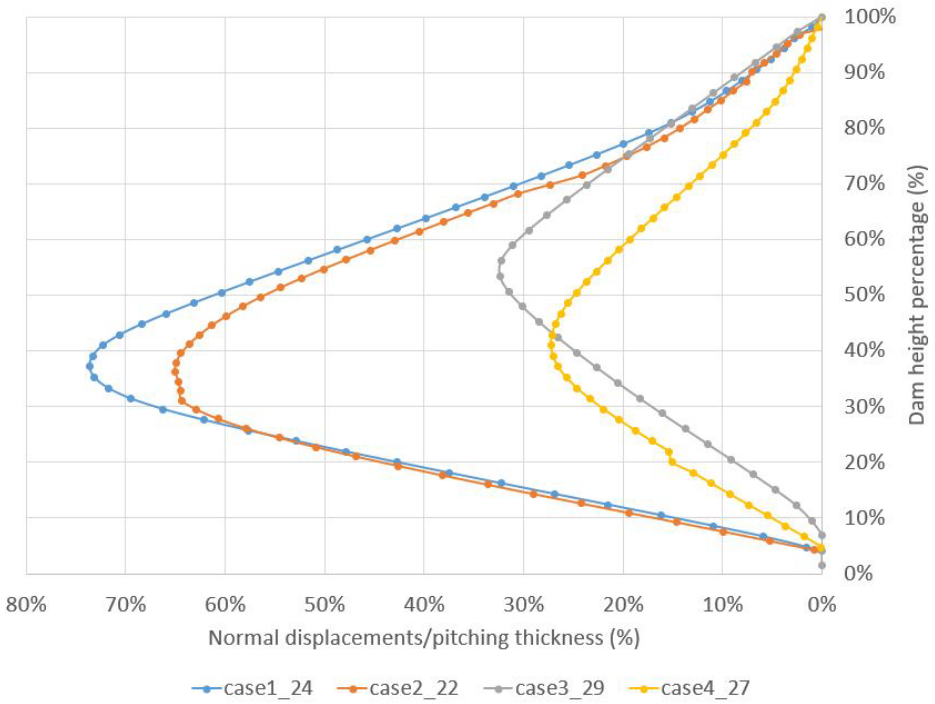

FIGURE 21 Simulations of PEDRA tests: normal normalized relative displacements for a rotation angle just before failure; case 1: 24°; case 2: 22°; case 3: 29°; case 4: 27°

$$F_\theta = \frac{tan(\alpha + \theta_{failure})}{tan(\alpha)} \tag{4}$$

The second safety factor F_ϕ is calculated by the reduction of one mechanical dam property. The main mechanical property that first explains the stability of the dam is the backfill friction angle ϕ. This safety factor is calculated by reducing the backfill friction angle until failure is reached (Equation 5).

The safety factors were computed on the basis of the rockfill dam using LKE model. Reduction of dam body resistance is provided by decreasing LKE model parameter a_{peak} until failure. Indeed, this parameter drives the value of the internal friction angle in LKE model. The internal friction angle $\phi_{equivalent}$ associated to a given value of a_{peak} is calculated. The safety factors were calculated for the four studied cases. An additional computation was processed considering a case for which the pitching was removed. This is a reference test that will indicate how much the pitching contributes to increase the dam stability. In the case of F_ϕ, calculations were carried out considering the pressure due to water in the reservoir ($F_{\phi(ww)}$, with water) on the pitching or without pressure ($F_{\phi(wow)}$, without water) using:

$$F_\phi = \frac{tan(\phi_{initial})}{tan(\phi_{reduced})} \tag{5}$$

All the calculated safety factors are shown in Table 7. Results firstly show that without pitching the rockfill dam is very close to failure according to both safety factors.

Secondly, the pitching induces a very good safety margin according to both safety factors. With respect to the reference case (without pitching), they are increased by a minimum factor of 2. Cases 3 and 4 lead to greater safety factors than cases 1 and 2. This is mainly due to a larger pitching weight. However, the weight of case 3 pitching is smaller than case 4 pitching while the safety factors are greater for the former. Therefore, backfill-pitching interface friction angle plays also an important role which actually was expected. Indeed, for retaining walls, such feature also holds true.

Case 1 is slightly more resistant than case 2 because of the higher resistance (contact friction angle) of granite blocks in the pitching compared to schist blocks in case 2 (Table 7). No conclusion can be drawn at this stage for the importance of its role since no computation was carried out with a very different kind of stones having a much higher or smaller contact friction angle.

One can refer to the study by Colas and al.[32] that studied the resistance of rockfill dams with a dry stone pitching. A parametric study was provided where failure was determined by means of the yield design method.

Finally, water of the reservoir has a little influence in the obtained results: failure is generally triggered in the one-third upper part of the dam where the hydrostatic pressure on the upstream face is rather low.

TABLE 7 Safety factors for the reference case with no pitching and for the four studied cases

	No pitching	Case 1	Case 2	Case 3	Case 4
F_θ	1.28	2.7	2.5	3.7	3.3
$F_{\phi(wow)}$	1.33	2.22	2.13	3.02	3.17
$F_{\phi(ww)}$	1.33	2.13	2.05	3.02	3.02

6 | CONCLUSION

This work provided a validation of the numerical modeling of rockfill dams with dry-stone pitching. It was based on the simulation of actual scaled-down pseudo-static tests where different properties for the pitching were investigated. Four cases from PEDRA campaign were analysed where differences lied in the kind of stones for the pitching, weight of pitching and the existence of anchored pitching blocks within the dam body. These cases were designed according to observations on site on actual rockfill dams with dry-stone pitching. The numerical model was built by coupling a DEM code with a FEM-like code. Two different constitutive models were used for the dam body, Mohr-Coulomb (MC) model and an advanced elasto-plastic model denoted LK-Enroch (LKE).

Irrespectively of the constitutive law for the dam body, the rotation angle leading to failure throughout tests in PEDRA campaign were retrieved with a very good precision. However, if a good prediction of the displacement field was obtained by means of LKE model, MC model unsuccessfully retrieved the correct displacement field due to its inherent stiff behavior. It lies in the existence of small initial elastic domain in LKE model that allows to generate irreversible deformations for small deviatoric stresses.

The relative displacements analysis of the pitching throughout simulations indicated the main role played by the backfill-pitching interface friction angle on the failure position. In addition, the role of the pitching weight on the dam's rigidity was also noticed. Increasing the dam weight tends to reduce the pitching deformations (normalized by the pitching thickness) at failure: the behavior of the dam is stiffer.

Two approaches were used to evaluate the safety factors of the studied dams. Both approaches justified quantitatively the main role played by the pitching in such dam's stability. The dam without pitching is close to failure with a safety factory slightly greater than 1. The safety factors increased to values higher than 2.5 for all the cases with pitching. Moreover, by comparing the four cases with pitching, the pitching weight and the interface friction angle were justified numerically to have a significant effect on the dam's resistance.

This work has shown a very small influence of water in the dam loading forces; however, one must remind that very different features and conditions can be at stake on actual structures. If the modeling of real rockfill dams was out of the scope of this study, such computations may quantitatively lead to very different results than obtained in this study. If the main qualitative conclusions related to the role of the pitching may hold true for actual dams, scale effect induced by far larger mean pressures in the dam body may greatly modify the quantities computed herein.

7 | APPENDIX 1: CONSTITUTIVE MODELING

7.1 | Backfill

Two constitutive models associated to the dam body are used. Their descriptions are presented in the upcoming subsections.

7.1.1 | Mohr-Coulomb

Mohr-Coulomb denoted MC is an elastic perfectly plastic constitutive model which is widely used in geotechnical computations for its simplicity. The associated failure surface is a straight cone. Its envelope in the deviatoric plane is given in Figure 22. Such model is mainly used for purely frictional soils (sand) and cohesive soils such as the clay and silt.

This model involves five parameters: friction angle ϕ, dilatancy angle ψ, cohesion C, Young's modulus E, and Poisson's ratio ν. They are usually obtained from triaxial tests by a trial-and-error method on the basis of deviatoric and volumetric curves (Figure 23).

The yield surface F which is also the failure surface reads:

$$F(\sigma_{ij}) = (\sigma_1 - \sigma_3) - (\sigma_1 + \sigma_3)sin\phi - 2Ccos\phi \tag{6}$$

where σ_1 and σ_3 are the major and minor principle stresses respectively.

The plastic potential G reads:

$$G(\sigma_{ij}) = (\sigma_1 - \sigma_3) - (\sigma_1 + \sigma_3)sin\psi \tag{7}$$

The flow rule is non-associated for granular soils which means friction angle ϕ and dilatancy angle ψ are different. Cohesion is equal to zero for purely frictional soils.

Although MC is widely used in soil modeling, it has several limits. For example, it does not take into account the effect of the pressure on the Young's modulus, friction angle and dilatancy angle. Moreover, the elastic domain is very large where no irreversible strains can be generated which do not reflect phenomena at stake in actual granular soils. It leads to the underestimation of deformations in the modeled systems. More sophisticated constitutive models may be required in that case.

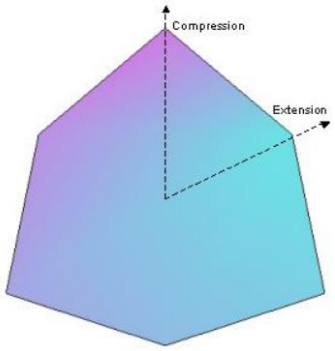

FIGURE 22 MC failure envelop in the deviatoric plane

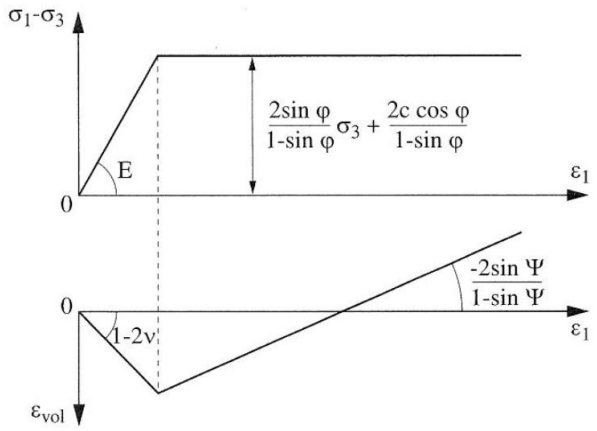

FIGURE 23 Simulation of a compression triaxial test using MC model[33]

7.1.2 | LK-Enroch

LK Enroch (LKE) model belongs to a class of constitutive models developed by EDF to address the short and long term modeling of rock formations, focusing mainly on underground structure such as tunnels.

LKE model was developed based on LK model specifically for rockfills. It considers a rock mass with zero cohesion which corresponds mechanically to the structure of rockfill from a rheological point of view. It is an elastoplastic model with two plastic deformation mechanisms, one which is isotropic and the other one is deviatoric (Equation 8). Hardening for both mechanisms is isotropic.

$$\dot{\varepsilon} = \dot{\varepsilon^e} + \dot{\varepsilon^p} and \dot{\varepsilon^p} = \dot{\varepsilon^{dp}} + \dot{\varepsilon^{ip}} \tag{8}$$

- Elastic mechanism

  The elastic mechanism is governed by two parameters: volumetric deformation modulus K and shear modulus G. The increment of elastic deformation can computed by:

$$\dot{\varepsilon^e_{ij}} = \frac{1+\nu}{E}\dot{\sigma_{ij}} - \frac{\nu}{E}\dot{I\delta_{ij}} \; or \; \dot{\varepsilon^e_{ij}} = \frac{1}{2G}\dot{s_{ij}} - \frac{1}{9K}\dot{I\delta_{ij}} \tag{9}$$

  K and G read:

$$K = K^e_0[\frac{I_1}{3P_a}]^{n_{elas}} \; and \; G = G^e_0[\frac{I_1}{3P_a}]^{n_{elas}} \tag{10}$$

  with K^e_0 and G^e_0 reference values for an effective mean pressure equal to $P_a = 100$kPa. I_1 is the first invariant of the effective stress tensor and n_{elas} is a model parameter.

- Plastic isotropic mechanism

  Concerning the plastic isotropic mechanism, the yield surface of the isotropic plastic mechanism is a plane orthogonal to the hydrostatic axis in the space of principal stresses, expressed by:

$$f^i(\sigma''; p_c) = \frac{I_1}{3} - p_c \tag{11}$$

  The hardening law is considered since the consolidation pressure p_c changes according to Equation 12. p_{c0} and β are model parameters and the volumetric plastic deformation ε^p_v is the hardening variable.

$$p_c = p_{c0}e^{\beta\varepsilon^p_v} \tag{12}$$

  The flow rule is associated (Equation 13) in which λ^i is the plastic multiplier of the isotropic mechanism.

$$\dot{\varepsilon^i_{ij}} = \dot{\lambda^i}\frac{\partial f^i}{\partial \sigma_{ij}} = \dot{\lambda^i}\frac{\delta_{ij}}{3} \tag{13}$$

- Plastic deviatoric mechanism

  Concerning the plastic deviatoric mechanism, LKE was developed on the base of Hoek and Brown rule[34], HB-CJS rule[35] and LK model. The deviatoric yield surface is mainly derived from the one of the original LK model. It is represented by Equation 14. It is adapted so that compression is at Lode angle $\theta = 0$.

$$f^d(\sigma_{ij}) = s_{II}h(\theta) - \sigma_c h^c_0[As_{II}h(\theta) + BI_1]^a = 0 \tag{14}$$

$$A = -\frac{mk}{\sqrt{6}\sigma_c h^c_0}; B = \frac{mk}{3\sigma_c}; K = (\frac{2}{3})^{\frac{1}{2a}}; s_{II} = \sqrt{2J_2} \tag{15}$$

$$h(\theta) = (1 - \gamma cos3\theta)^{1/6}; h_0^c = h(0); h_0^e = h(\pi/3) \tag{16}$$

The hardening variable of the elastoplastic mechanism is the deviatoric plastic deformation γ^d defined by:

$$\gamma^d = \int (\frac{2}{3} e_{ij}^{\dot{d}} . e_{ij}^{\dot{d}})^{1/2} dt, \ where \ e_{ij}^{\dot{d}} = \varepsilon_{ij}^{\dot{d}} - \frac{\varepsilon_v^{\dot{d}}}{3} \delta_{ij} \ and \ \varepsilon_v^{\dot{d}} = \varepsilon_{kk}^{\dot{d}} \tag{17}$$

For each parameter a and m involved in equations 14 and 15, specific variation laws are defined according to the hardening variable γ^d: the elastoplastic surface thus evolves throughout different reference state, manely the peak state and the residual state at large deformations. The different hardening phases are bounded by "threshold" values, noted γ_{peak} and γ_{res} .

In the pre-peak phase, the deviatoric yield surface evolves from the elasticity threshold to the peak threshold, for $0<\gamma^d<\gamma_{peak}$, according to the following laws (X_{ams} is a model parameter):

$$a(\gamma^d) = a_0 + ln(1 + \frac{\gamma^d}{X_{ams}\gamma_{peak}})(\frac{a_{peak} - a_0}{ln(1 + 1/X_{ams})}) \tag{18}$$

$$m(\gamma^d) = m_0 + ln(1 + \frac{\gamma^d}{X_{ams}\gamma_{peak}})(\frac{m_{peak} - m_0}{ln(1 + 1/X_{ams})}) \tag{19}$$

Throughout the post-peak phase, the deviatoric yield surface evolves from the peak threshold to the residual threshold, for $\gamma_{peak}<\gamma^d<\gamma_{res}$, according to:

$$a(\gamma^d) = a_{peak} + ln(1 + \frac{1}{\eta}\frac{\gamma^d - \gamma_{peak}}{\gamma_{res} - \gamma_{peak}})(\frac{1 - a_{peak}}{ln(1 + 1/\eta)}) \tag{20}$$

$$m(\gamma^d) = \frac{\sigma_c}{\sigma_{pt}}(m_{peak}\frac{\sigma_{pt}}{\sigma_c})^{\frac{a_{peak}}{a(\gamma^d)}} \tag{21}$$

η is a model parameter while σ_{pt} corresponds to the abscissa of the intersection point of the peak and residual thresholds, in the plane (σ_{min}; σ_{max}). It is determined analytically by:

$$\sigma_{pt} = (\frac{m_{res}\sigma_c^{a_{peak}-1}}{m_{peak}^{a_{peak}}})^{\frac{1}{a_{peak}-1}} \tag{22}$$

The deviatoric deformations are obtained from the following expression:

$$\varepsilon_{ij}^{\dot{d}} = \lambda^{\dot{d}} G_{ij} \tag{23}$$

Where G is the hardening function of the elastoplastic mechanism defined by:

$$G_{ij} = \frac{\partial f^d}{\partial \sigma_{ij}} - (\frac{\partial f^d}{\partial \sigma_{kl}} n_{kl}) n_{ij} \tag{24}$$

$$n_{ij} = \frac{\beta' \frac{s_{ij}}{s_{II}} - \delta_{ij}}{\sqrt{\beta'^2 + 3}}, \ where \ \beta' = \frac{\sqrt{6} g_v}{3 - g_v} \ and \ g_v = -\frac{2sin\psi}{1 - sin\psi} \tag{25}$$

λ^d represents the plastic multiplier of the deviatoric mechanism. More details associated to LKE model can be found in [25]

A triaxial test representation using LKE model (stress-strain curve) is given in Figure 24. One can notice that the curve is split into four different domains. The first one is the elastic domain (0) in which reversible deformations are observed. Then, plastic hardening domain (1) starts with plastic deformations until it reaches the peak deviatoric stress value: until this point, the volumetric behavior is mostly contractive. At peak, the softening domain (2) starts with dilative volumetric behavior until it reaches the residual domain (3) which corresponds to the critical state.

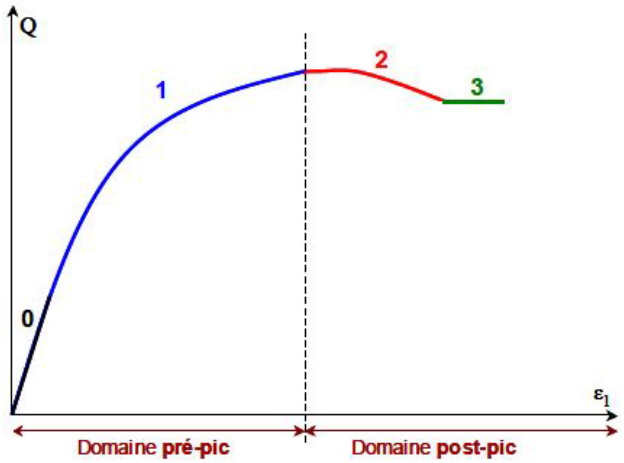

FIGURE 24 Deviatoric triaxial behavior using LKE model

TABLE 8 LKE model with its sixteen parameters definition

General Parameters			
E	Young Modulus (Pa)	ν	Poisson's ratio
n_{elas}	Exponent of the law of variation of elastic moduli K and G	σ_c	Simple compressive strength (Pa)
Elasticity threshold parameters			
a_0	Elasticity threshold a	m_0	Elasticity threshold m
Peak parameters			
m_{peak}	Peak threshold a	m_{peak}	Peak threshold a
Hardening parameters			
$\dot{\gamma}_{peak}$	Strain rate from the elasticity to peak threshold	$\dot{\gamma}_{res}$	Strain from the elasticity to peak threshold
X_{ams}	Parameter involved in the pre-peak hardening laws	μ	Parameter involved in the post-peak hardening laws
Volumetric deformation parameters			
ϕ_{res}	Residual friction angle (°)	ψ_0	Dilatancy angle of the Phase Transformation state
Isotropic mechanism parameters			
p_{c0}	Initial consolidation pressure	β	Parameter involved in the isotropic hardening laws

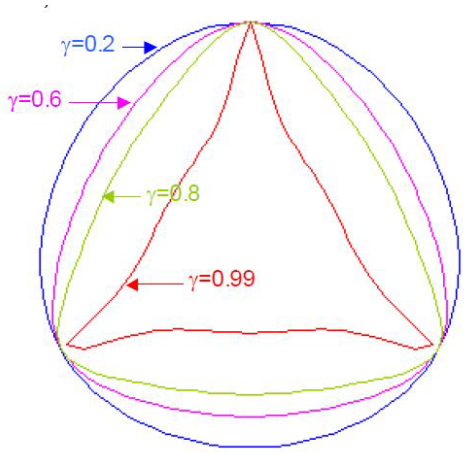

FIGURE 25 LKE deviatoric failure envelop in the deviatoric plane

In total, LKE model has sixteen input parameters, divided into several groups with their own effects on the behavior. They are all given in Table 8 with their definitions. Some parameters are typical and are required for most of the soil models such as E, ν, σ_c, ϕ, and ψ.

An extra parameter is also found which is the shape factor parameter (disymmetry) γ. In Figure 25, the failure envelope of LKE is shown: different disymmetry cases are plotted when playing with the shape factor parameter γ. More detailed description of this model can be found in the PhD thesis of Chen[25].

Identifying those model parameters usually needs experimental data from triaxial and oedometric tests. The main problem in this process is the lack of experimental data to be based on due to difficulty in carrying out experiments on large samples of rockfill or due to the lack of access to this data. To overcome the lack of data, the literature and previous studies can be helpful in identifying those parameters.

7.2 | Linear frictional contact model

A linear frictional model is used to model the contacts between the blocks and at the interface. This model is composed of two components that act in parallel with each other: the first one is the linear component which provides the linear elastic frictional behavior with no tension whereas the second is the dashpot component which provides viscous behavior (Equation 26).

Each component is split into normal and shear forces (Equation 27). The linear force is calculated using the linear springs with constant normal and shear stiffnesses k_n and k_s. The dashpot force is calculated using dashpots with normal and shear critical damping ratios β_n and β_s. The contact can be considered as active or inactive according to the gap between two different bodies. The surface gap g_s is the difference between the contact gaps g_c and the reference gap g_r. The contact is active only if the surface gap is less than or equal to zero. The contact interface consists of a contact plane with certain position and normal direction. It is centered in the overlapping volume or gap and it is tangent to the two contact surfaces. Detailed diagram of the linear model is shown in Figure 26. In the case of inactive dashpots and zero reference gap, this model corresponds to the model of Cundal[23].

$$F_c = F^l + F^d \tag{26}$$

$$F^l = -F_n^l \hat{n_c} + F_s^l \ , \ F^d = -F_n^d \hat{n_c} + F_s^d \tag{27}$$

The force displacement law is used to calculate the contact forces at each active contact (Figure 27). The force is updated according to the relative displacement increment. The linear normal force is updated based on the normal displacement (surface gap) increment $\Delta\delta_n$. Moreover, no tension forces exits in this linear model. The linear shear force is updated based on the relative shear displacement increment $\Delta\delta_s$. This shear force can increase with the relative shear displacement until a threshold then slipping behavior occurs. If the contact changes from being inactive to active during the current timestep, just the amount of this increment that takes place while the surface gap is negative is employed to carry out the incremental update of the normal and

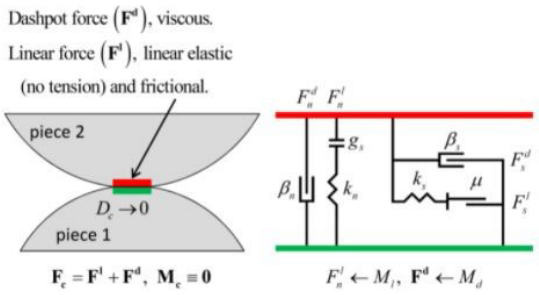

FIGURE 26 Behavior and rheological components of the linear model

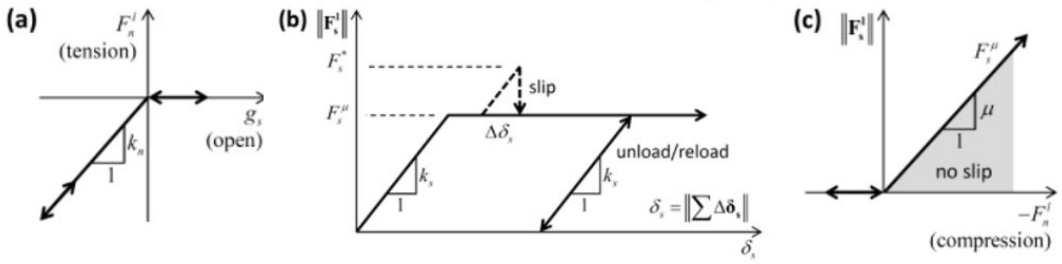

FIGURE 27 Force-displacement law for the linear component of the unbonded linear-based models: (a) normal force versus surface gap, (b) shear force versus relative shear displacement, and (c) slip envelope

shear forces. The dashpot forces are also updated based on the dashpot mode and incremental equations. Detailed description can be found in ITASCA $PFC3D$ documentation[36].

8 | APPENDIX 2: HICHER AND RAHMA APPROACH

An analytical approach was developed and validated on triaxial experimental tests by Hicher and Rahma[30] to determine several model parameters of granular materials including the preconsolidation pressure p_{c0} and β. The analytical equations used to calculate those two parameters are the following:

$$log(p_{c,min}) = -12log\ C_z - 4.7e_{e_{max}} + 9.71I_e + 2.2\ \pm 0.5 \qquad R = 0.96 \tag{28}$$

$$log(p_{c,max}) = -4log\ C_U - 7.5e_{e_{min}} + 4.75I_e + 7.1\ \pm 0.3 \qquad R = 0.95 \tag{29}$$

$$\beta_{norm} = (log(p_{c,max}) - log(p_{c,min})) \tag{30}$$

$$\beta = \frac{2.3\beta_{norm}(1+e_0)}{I_e} \tag{31}$$

Where:

- $C_u = D_{60}/D_{10}$ is the coefficient of uniformity
- $C_z = \frac{D_{30}^2}{D_{60}.D_{10}}$
- e_{max} and e_{min} are the maximum and minimum void ratios respectively of the studied granular material. They can be obtained from previous studies[37].
- $I_e = e_{max} - e_{min}$; relative density $D_r = \frac{e_{max}-e_0}{e_{max}-e_{min}}$
- $p_{c,max}$ and $p_{c,min}$ are two specific values for p_c corresponding to two different void ratios e_{max} and e_{min} respectively

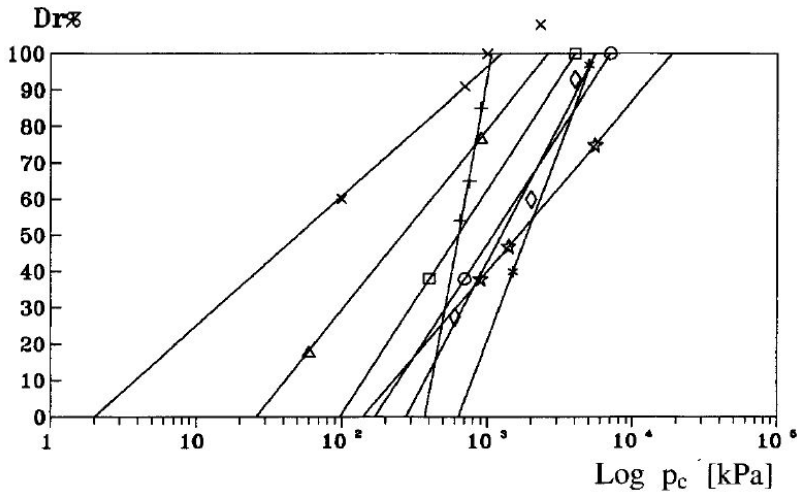

FIGURE 28 ($log(p_c)$, D_r) plane

Knowing the values of $log(p_{c,min})$ and $log(p_{c,max})$, a straight line can be drawn in ($log(p_c)$, D_r) plane as shown in Figure 28. Then, the value of p_{c0} can be deduced from this line at a given relative density D_r corresponding to a void ratio e_0. More details about this approach can be found in its dedicated article[30].

9 | APPENDIX 3: DISPLACEMENTS OF CASES 1, 2 AND 3

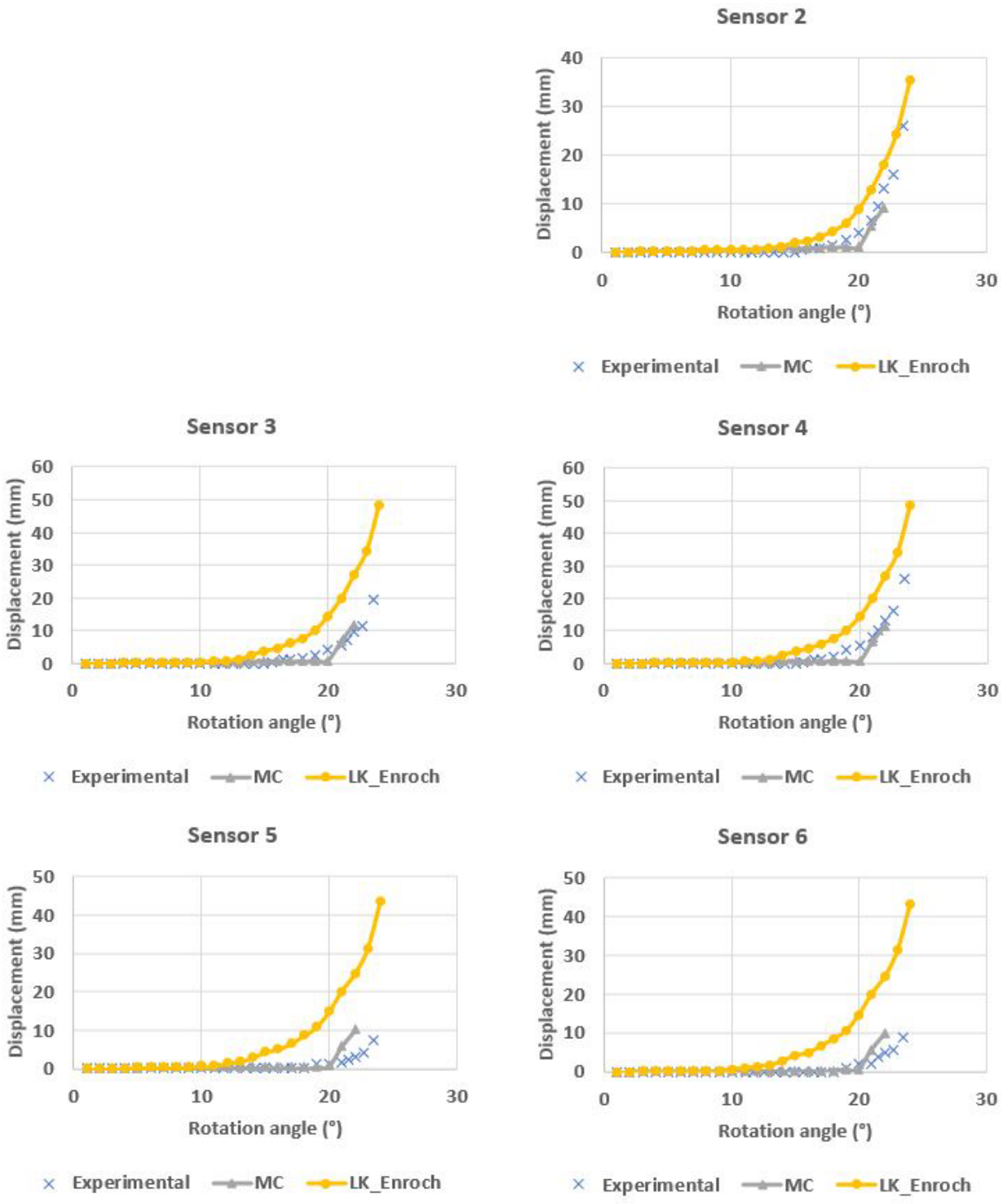

FIGURE 29 Displacements at the 6 sensors of the downstream face of case 1

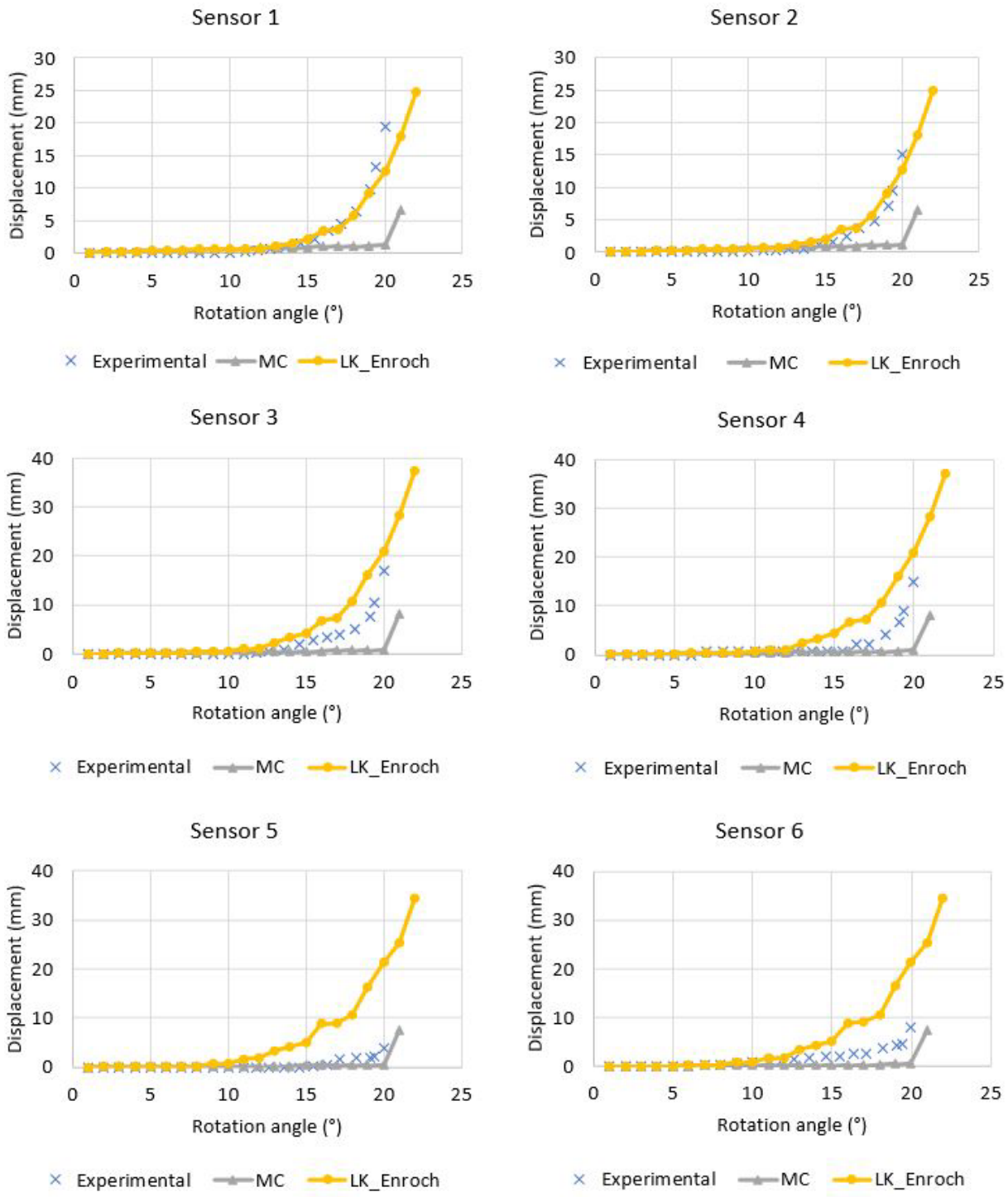

FIGURE 30 Displacements at the 6 sensors of the downstream face of case 2

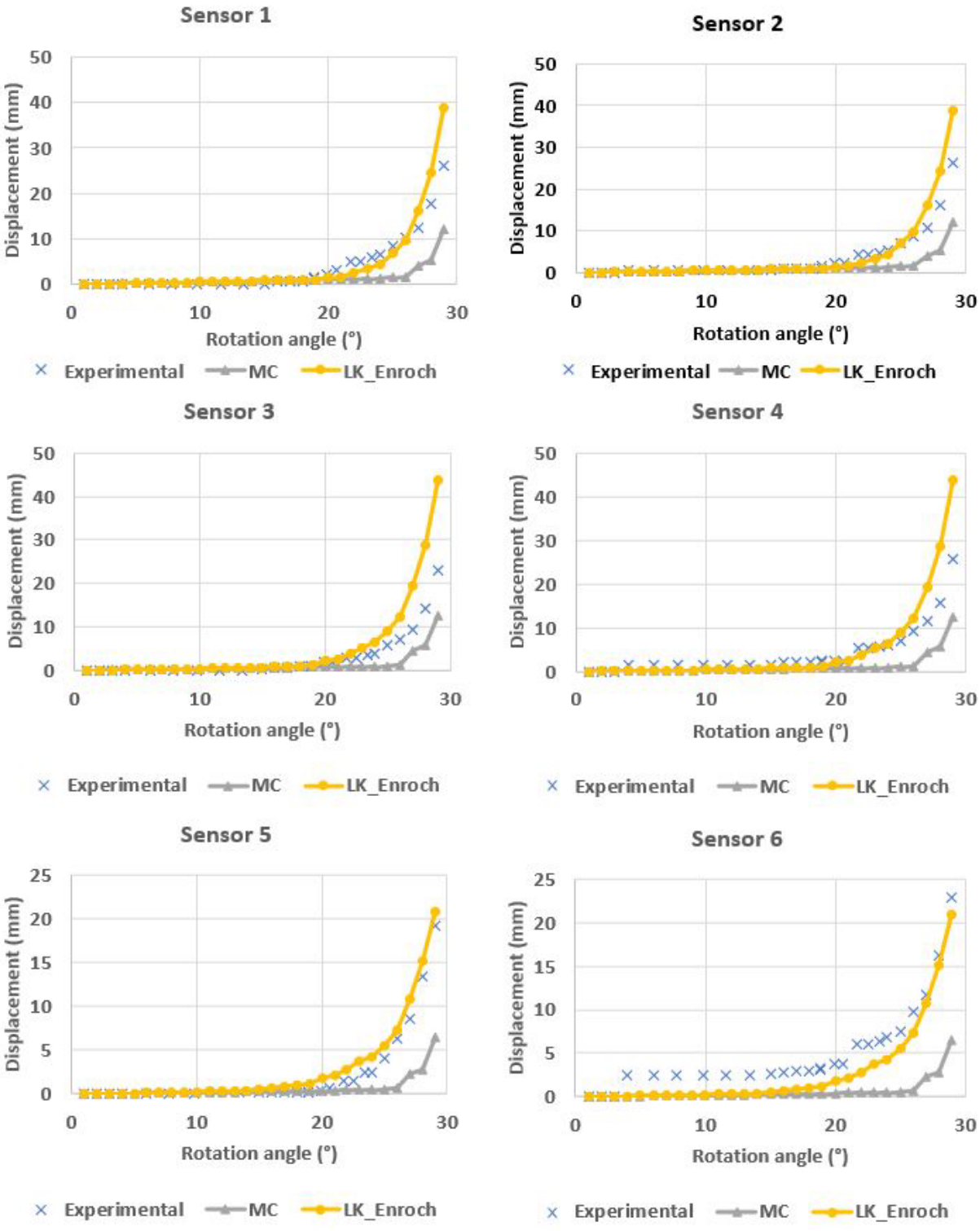

FIGURE 31 Displacements at the 6 sensors of the downstream face of case 3

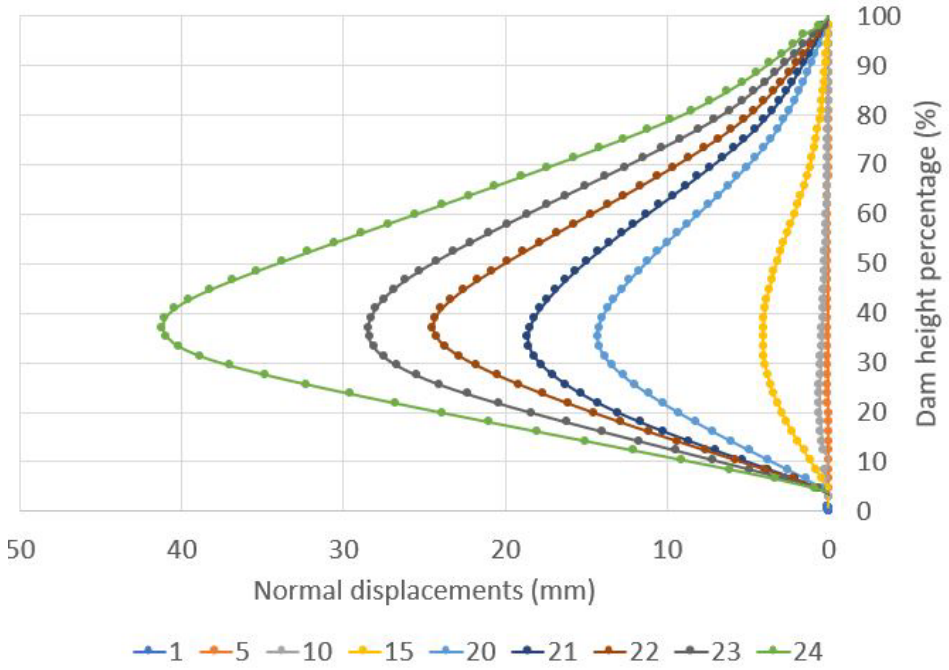

FIGURE 32 Normal relative displacements evolution of the pitching throughout the tilting tests; simulation of case 1

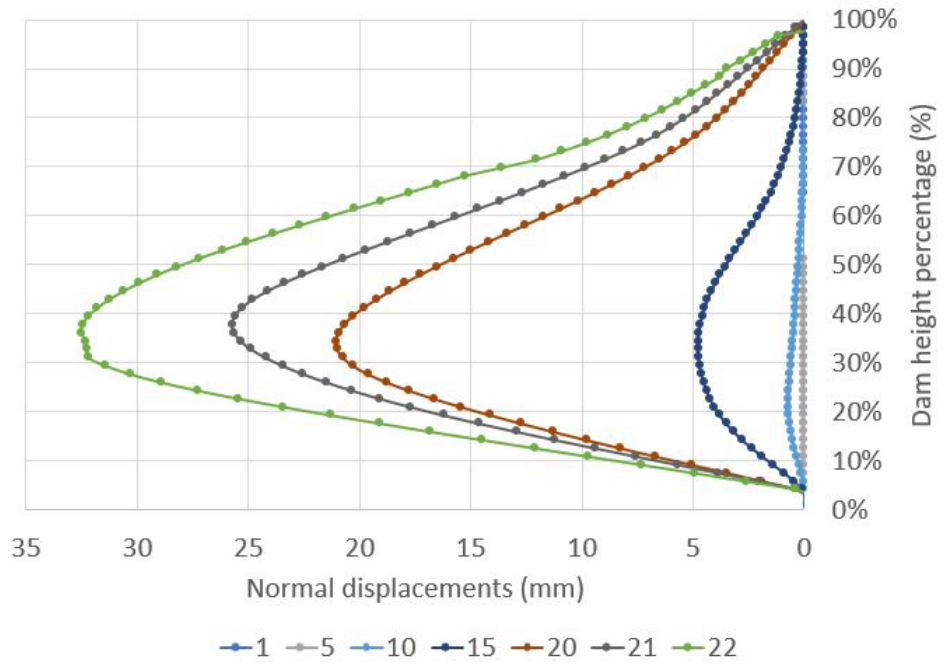

FIGURE 33 Normal relative displacements evolution of the pitching throughout the tilting tests; simulation of case 2

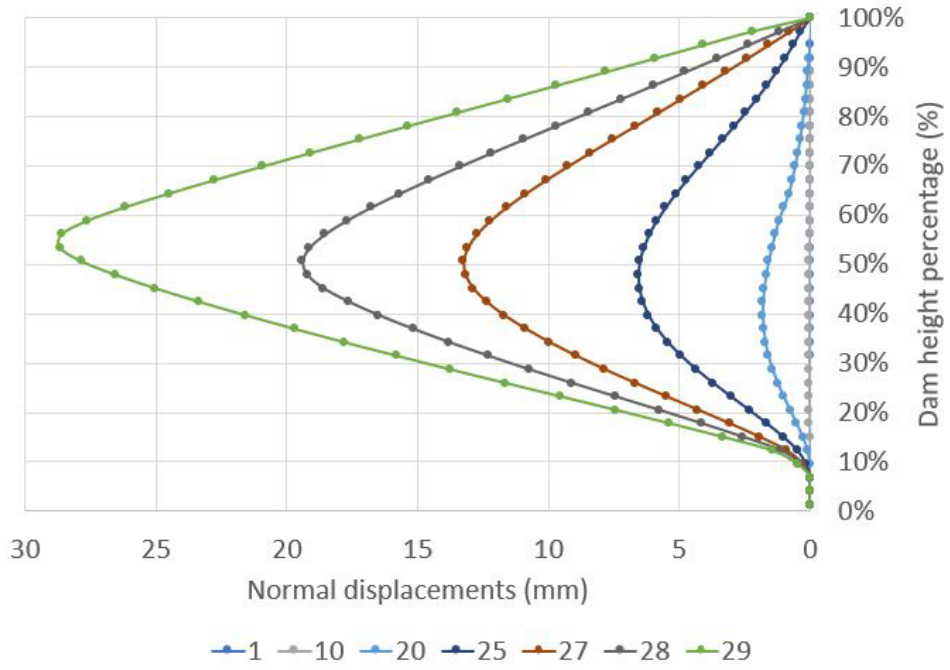

FIGURE 34 Normal relative displacements evolution of the pitching throughout the tilting tests; simulation of case 3

ACKNOWLEDGMENTS

The authors acknowledge EDF – Center of Hydraulic Engineering that funded both the experimental campaign that allowed the validation of the numerical model to be performed and the research work presented in this paper.

References

1. Kerisel J. History of retaining wall design. In: Thomas Telford Publishing. 1993 (pp. 1–16).
2. Thew I, Sutherland A, Theodossopoulos D. Structural response of drystone Iron Age brochs. *Proceedings of the Institution of Civil Engineers-Structures and Buildings* 2013; 166(6): 316–324.
3. Schnitter NJ. *A history of dams: the useful pyramids*. Balkema Rotterdam . 1994.
4. Coyne ALJ. *Leçons sur les grands barrages*. École nationale des ponts et chaussées . 1943.
5. Anon . Experiments carried on at Chatham by the late Lieutenant Hope, Royal Engineers, on the pressure of earth against revetments, and the best form of retaining walls. *Corps R. Eng.* 1845;(7): 64–86.
6. Burgoyne . Revetments of retaining walls. *Corps R. Eng.* 1853;(3): 154–159.
7. Colas AS, Morel JC, Garnier D. Full-scale field trials to assess dry-stone retaining wall stability. *Engineering Structures* 2010; 32(5): 1215–1222.
8. Colas AS, Morel JC, Garnier D. Assessing the two-dimensional behaviour of drystone retaining walls by full-scale experiments and yield design simulation. *Géotechnique* 2013; 63(2): 107–117.
9. Villemus B, Morel J, Boutin C. Experimental assessment of dry stone retaining wall stability on a rigid foundation. *Engineering structures* 2007; 29(9): 2124–2132.
10. Mundell C, McCombie P, Heath A, Harkness J, Walker P. Behaviour of drystone retaining structures. *Proceedings of the Institution of Civil Engineers-Structures and Buildings* 2010; 163(1): 3–12.
11. Mundell C, McCombie P, Bailey C, Heath A, Walker P. Limit-equilibrium assessment of drystone retaining structures. *Proceedings of the Institution of Civil Engineers-Geotechnical Engineering* 2009; 162(4): 203–212.
12. Savalle N, Vincens É, Hans S. Experimental and numerical studies on scaled-down dry-joint retaining walls: Pseudo-static approach to quantify the resistance of a dry-joint brick retaining wall. *Bulletin of Earthquake Engineering* 2020; 18(2): 581–606.
13. Colas A, Morel J, Garnier D. Yield design of dry-stone masonry retaining structures—Comparisons with analytical, numerical, and experimental data. *International journal for numerical and analytical methods in geomechanics* 2008; 32(14): 1817–1832.
14. Colas AS, Garnier D, Morel JC. Yield design modelling of dry joint retaining structures. *Construction and Building Materials* 2013; 41: 912–917.
15. Alejano L, Veiga M, Gómez-Márquez I, Taboada J. Stability of granite drystone masonry retaining walls: II. Relevant parameters and analytical and numerical studies of real walls. *Géotechnique* 2012; 62(11): 1027–1040.
16. Alejano L, Veiga M, Taboada J, Díez-Farto M. Stability of granite drystone masonry retaining walls: I. Analytical design. *Géotechnique* 2012; 62(11): 1013–1025.
17. Kim SS, Mok YJ, Jung YH. Behavior of dry-stone segmental retaining wall using physical modeling and numerical simulation. *Journal of the Korean Geotechnical Society* 2011; 27(9): 25–36.
18. Terrade B, Colas AS, Garnier D. Upper bound limit analysis of masonry retaining walls using PIV velocity fields. *Meccanica* 2018; 53(7): 1661–1672.

19. Oetomo J, Vincens E, Dedecker F, Morel JC. Modeling the two-dimensional failure of dry-stone retaining wall. In: IC2E International Centre for Computational Engineering. ; 2013: 717–725.

20. Oetomo JJ, Vincens E, Dedecker F, Morel JC. Modeling the 2D behavior of dry-stone retaining walls by a fully discrete element method. *International journal for numerical and analytical methods in geomechanics* 2016; 40(7): 1099–1120.

21. Deluzarche R. *Modélisation discrète des enrochements: Application aux barrages*. PhD thesis. Ecully, Ecole centrale de Lyon, 2004.

22. Deluzarche R. Discrete modelling of rock-fill: Application to dams; Modelisation discrete des enrochements: Application aux barrages. 2004.

23. Cundall PA, Strack OD. A discrete numerical model for granular assemblies. *geotechnique* 1979; 29(1): 47–65.

24. Itasca C. PFC-2D, Particle Flow Code in 2 Dimensions. *Theory and Background. Itasca* 2002; 708.

25. Chen Y. *Modélisation du comportement mécanique des grands CFRD: Identification des caractéristiques des enrochements et comportement du masque d'étanchéité amont*. PhD thesis. Ecole Centrale de Lyon, 2012.

26. Oetomo J. *Comportement des murs de soutènement en pierre sèche: une modélisation par approche discrète*. PhD thesis. Ecully, Ecole centrale de Lyon, 2014.

27. Savalle N, Vincens E, Dedecker F. DEM MODELLING OF DRY STONE RETAINING WALLS.

28. Leps TM. Review of shearing strength of rockfill. *Journal of the Soil Mechanics and Foundations Division* 1970; 96(4): 1159–1170.

29. Bolton M. The strength and dilatancy of sands. *Geotechnique* 1986; 36(1): 65–78.

30. Hicher P, Rahma A. Micro-macro correlations for granular media. Application to the modelling of sands. *European Journal of Mechanics. A. Solids* 1994; 13.

31. Ozturk C, Nasuf E. Strength Classification of Rock Material Based on Textural Properties. *Tunnelling and Underground Space Technology* 2013; 37: 45-54. doi: 10.1016/j.tust.2013.03.005

32. Colas AS, Morel JC, Garnier D. Upper-bound solution for the stability of stone-facing embankments. *Materials and Structures* 2016; 49(10): 4279–4289.

33. Hicher P, Shao J. Elastoplasticite des sols et des roches. *Modèles de comportement des sols et des roches* 2002; 1.

34. Hoek E, Carranza-Torres C, Corkum B, others . Hoek-Brown failure criterion-2002 edition. *Proceedings of NARMS-Tac* 2002; 1(1): 267–273.

35. Cambou B, Jafari K, Elamrani K. An elastoplastic model for granular material using three yielding mechanisms. In: ; 1989: 1–8.

36. Itasca C. Pfc3d (particle flow code in 3 dimensions), version 4.0. *Minneapolis: ICG* 2008; 3.

37. Biarez J, Hicher PY. Influence de la granulométrie et de son évolution par ruptures de grains sur le comportement mécanique de matériaux granulaires. *Revue française de génie civil* 1997; 1(4): 607–631.

How to cite this article: Haidar A, Vincens E, and Dedecker F. FEM-DEM modeling of pseudo static experiments on scaled-down rockfill dams with dry stone pitching, *2021;00:10–19*.